Development of a metal-free black phosphorus/graphitic carbon nitride heterostructure for visible-light-driven degradation of indomethacin

He, D.Y.; Jin, D.X.; Cheng, F.Y.; Zhang, T.T.; Qu, J.; Zhou, Y.J.; ... ; Peijnenburg, W.J.G.M.

Science of the Total Environment 804 (2022) 150062

Contents lists available at ScienceDirect

Science of the Total Environment

journal homepage: www.elsevier.com/locate/scitotenv

Development of a metal-free black phosphorus/graphitic carbon nitride heterostructure for visible-light-driven degradation of indomethacin

Dongyang He [a,1], Dexin Jin [a,1], Fangyuan Cheng [a], Tingting Zhang [a], Jiao Qu [a,*], Yangjian Zhou [b], Xing Yuan [a], Ya-nan Zhang [a], Willie J.G.M. Peijnenburg [c,d]

[a] School of Environment, Northeast Normal University, Changchun, Jilin 130117, China
[b] School of Environmental Science and Engineering, Guangdong Provincial Key Laboratory of Environmental Pollution Control and Remediation Technology, Sun Yat-sen University, Guangzhou 510275, China
[c] Institute of Environmental Sciences, Leiden University, Leiden, the Netherlands
[d] National Institute of Public Health and the Environment (RIVM), Bilthoven, the Netherlands

HIGHLIGHTS

- A low-cost BP-g-C_3N_4 photocatalyst is fabricated via a newly-developed strategy.
- The BP-g-C_3N_4 significantly outperforms the P25 TiO_2 under natural sunlight.
- Mechanism for the enhanced photocatalytic activity is proposed.
- Effect of natural water constituents and water matrices is studied.

GRAPHICAL ABSTRACT

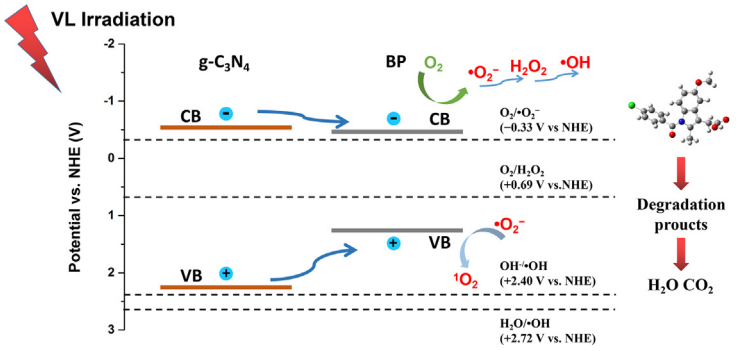

ARTICLE INFO

Article history:
Received 8 July 2021
Received in revised form 27 August 2021
Accepted 27 August 2021
Available online 7 September 2021

Editor: Yifeng Zhang

Keywords:
Pharmaceuticals and personal care products
Graphitic carbon nitride
Black phosphorus
Photocatalysis

ABSTRACT

The development of affordable and efficient technologies for the removal of pharmaceuticals and personal care products (PPCPs) from water has recently been the subject of extensive attention. In this study, a black phosphorus/graphitic carbon nitride (BP-g-C_3N_4) heterostructure is fabricated as an extremely active metal-free photocatalyst via a newly-developed exfoliation strategy. The BP-g-C_3N_4 shows an 11 times better decomposition rate of a representative PPCPs-type pollutant, indomethacin (IDM), compared to the widely-used P25 TiO_2 under real-sunlight illumination. Also, its visible-light activity is even better than that of the best photocatalysts previously developed, but only consumes 1/10–1/4 of the catalyst. The results show that BP performs a cocatalyst-like behavior to catalyze the generation of reactive oxygen species, thus speeding up the decomposition of IDM. In addition, the BP-g-C_3N_4 photocatalyst also exhibits excellent IDM removal efficiency in authentic water matrices (tap water, surface water, and secondarily treated sewage effluent). Large-scale application demonstration under natural sunlight further reveals the practicality of BP-g-C_3N_4 for real-world water treatment operations. Our work will open up new possibilities in the development of purely metal-free photocatalysts for "green" environmental remediation applications.

1. Introduction

In recent decades, pharmaceuticals and personal care products (PPCPs) have been categorized as contaminants of growing concern

* Corresponding author.
E-mail address: quj100@nenu.edu.cn (J. Qu).
[1] These authors contributed equally to this work.

https://doi.org/10.1016/j.scitotenv.2021.150062
0048-9697/

due to their widespread occurrence in surface water, ground water, drinking water, and sewage [Archer et al., 2017]. The residues of these compounds, with largely unknown chronic effects, may easily result in severe problems to man and the environment. Unfortunately, conventional sewage treatment plants, which have been identified as the primary source of PPCPs in aquatic systems, are not efficient enough in removing PPCPs, as these plants are not designed specifically for such pollutants [Liu and Wong, 2013]. Since the residues of PPCPs have already been detected in our food chain, it is urgently needed to develop efficient techniques for the removal of PPCPs, of which semiconductor photocatalysis has been considered as a promising one [Yang et al., 2017]. A low-cost and high-performance photocatalyst is the key to advance this technology into real-world water treatment operations. Unfortunately, despite extensive efforts during the past few decades, most of the reported photocatalysts still face several challenging problems: (1) the solar energy utilization ability of the mostly-studied photocatalysts is far from satisfactory [e.g., TiO_2 has a bandgap of 3.0–3.2 eV and can only be excited by ultra-violet (UV) light, which accounts only for 4% of the solar energy]; (2) many photocatalysts are composed of rare and expensive materials; (3) the photocatalysts made of earth-abundant and low-cost materials exhibit in general insufficient photocatalytic efficiency [Jiang et al., 2019; Moniz et al., 2015; Wu et al., 2020; Zhang et al., 2019].

Graphitic carbon nitride (g-C_3N_4), as a typical metal-free semiconductor with a visible-light (VL) driven bandgap, grabs tremendous attention owing to its simple synthesis, low cost, nontoxic nature, as well as earth-abundant and environmental-friendly chemical composition [Fei et al., 2021; Han et al., 2018; Ong et al., 2016; Wang et al., 2018b]. However, pure g-C_3N_4 exhibits only limited photoactivity due to its poor charge carrier separation efficiency [Sun et al., 2017]. Introducing cocatalysts into g-C_3N_4 systems is the most common strategy for the photoactivity improvement of g-C_3N_4 materials. Noble metals, such as Ag, Au, Pt, and Pd have been confirmed to be the most efficient cocatalysts for g-C_3N_4, as they can form metal-semiconductor junctions with g-C_3N_4, thus facilitating the separation of photo-induced charge carriers [Chang et al., 2013; Cheng et al., 2013; Ma et al., 2016; Xue et al., 2015]. However, these noble metals suffer from high price and limited reserve, which is clearly incongruent with the cost-effective and environmentally friendly viewpoint. What is worse, it has been shown in literature that the noble-metal-containing photocatalysts may result in secondary pollution due to the leakage of metallic ions [Hu et al., 2010; Zhang et al., 2010]. To this end, suitable materials as cocatalysts are expected to be highly efficient and be composed of environmentally benign non-metal elements.

Phosphorus is one of the most abundant elements on earth [Liu et al., 2015]. As the most thermodynamically stable allotrope of phosphorus, black phosphorus (BP), has sparked increasing research interests as an emerging two-dimensional (2D) semiconductor [Eswaraiah et al., 2016]. Recently, few-layer BP has been found to be a potential high-performance cocatalyst to replace noble metals due to its prominent properties of (1) large surface area with efficient exposure of active sites; (2) layer-dependent direct bandgap ranging from 0.3 to 2.0 eV; (3) excellent charge mobility of 1000 $cm^2\ V^{-1}\ S^{-1}$; (4) strong optical absorption from the UV to the near-infrared region [Batmunkh et al., 2016; Lewis et al., 2017; Meng et al., 2021; Zhao et al., 2018; Zhou et al., 2021; Zhu et al., 2017]. Weng's group prepared a hybrid photocatalyst composed of zeolitic imidazolate framework-8 (ZIF-8) and BP for the photocatalytic decomposition of methylene blue, in which the activity of ZIF-8 was significantly improved after the hybridization with BP [Wang et al., 2016]. Qiao's group reported photocatalytic H_2 production by using a BP/CdS photocatalyst with BP acting as the cocatalyst, and the activity was found to be even higher than that of the Pt/CdS photocatalyst [Ran et al., 2017]. However, to the best of our knowledge, the potential of using BP as a metal-free cocatalyst to replace precious metals for the catalytic removal of PPCPs has not been explored.

Very recently, some researchers have constructed 2D/2D BP-g-C_3N_4 heterostructures with enhanced photocatalytic activity, using the liquid-phase exfoliation (LPE) method (a widely-used strategy for the construction of 2D/2D heterostructure photocatalysts). For instance, Jiang's group developed a BP nanosheets decorated g-C_3N_4 nanosheets photocatalyst by using a water-based LPE method followed by a calcination process, for photocatalytic nitrogen fixation [Qiu et al., 2018]. Wang's group synthesized a BP-g-C_3N_4 hybrid photocatalyst by a one-pot LPE strategy in the medium of *N*-methyl-2-pyrrolidone (NMP), for photocatalytic molecular oxygen activation [Zheng et al., 2018]. The major merit of the LPE method is that it provides an avenue for the simple synthesis of high-efficiency 2D/2D composite materials, as the intimate "face to face" contact can be established to enhance the interfacial charge separation when two bulk structures are concurrently exfoliated to nanosheets [Zheng et al., 2020a]. However, it seems impractical for one pure exfoliation medium to be a satisfactory liquid system for both g-C_3N_4 and BP. Successful exfoliation requires minimizing the enthalpy of the mixing based on a match between the surface energy of the solvent and the material, while the surface energy of g-C_3N_4 and BP is different [Hernandez et al., 2008; Mu and Si, 2015; Yang et al., 2013]. Thus, exploring a novel method to produce high-performance 2D/2D BP-g-C_3N_4 heterostructures still remains a strenuous task.

In this paper, for the first time, a 2D/2D BP-g-C_3N_4 photocatalyst is facilely prepared by a newly-developed single-step LPE strategy in a binary azeotrope, and firstly used as a metal-free heterostructure for the photocatalytic removal of PPCPs. As one of the most damaging non-steroid anti-inflammatory drug, indomethacin (IDM) has widely been detected in sewage and surface water owing to the poor removal efficiency of contemporary wastewater treatment technologies, and thus it is chosen as a representative PPCPs-type pollutant in this study [Zhao et al., 2017]. The photoactivity of BP-g-C_3N_4 toward the removal of IDM is investigated under VL irradiation, and the mechanism for enhanced photoactivity of BP-g-C_3N_4 is systematically studied. Additionally, possible photocatalytic mechanism and potential catalytic pathways of IDM are also explored to better understand the BP-g-C_3N_4 photocatalytic system. Subsequently, the feasibility of BP-g-C_3N_4 for practical water treatment applications is studied by the decomposition of IDM in authentic water matrices, with mixed natural water constituents, and under real-sunlight irradiation. This study provides ideas for the development of metal-free efficient heterostructures for real-world photocatalytic environmental remediation applications.

2. Experimental methods

2.1. Solvent survey

In a typical procedure, 20 mg of g-C_3N_4 (10 mg for BP) powder was dispersed in 20 mL of corresponding solvent (ethanol solutions, water, and NMP). The mixed solution was then ultrasonically exfoliated for 90 min in a water bath sonication. After centrifuging at 750 rpm (500 rpm for BP) for 30 min, the supernatant was collected and the amount of dispersed g-C_3N_4 (or BP) nanosheets was measured by using a UV–vis spectrophotometer (Hitachi U-2900) at a wavelength of 660 nm.

2.2. Preparation of the BP-g-C_3N_4 heterostructure photocatalyst

The BP-g-C_3N_4 heterostructure photocatalyst was prepared by a facile LPE method. In detail, 100 mg of bulk g-C_3N_4 and different amounts of bulk BP were added into a binary azeotrope composed of ethanol and water (v:v = 2:3, total volume = 20 mL). Then, the mixture solution was bubbled with N_2 for 15 min, followed by ice-bath sonication for 8 h. After that, the product was collected using high-speed centrifugation, followed by drying at 60 °C for 12 h in a vacuum oven. The weight ratios of BP to g-C_3N_4 were 1, 4, 8, and 12 wt%, and the corresponding BP-g-C_3N_4 samples were denoted as 1%BP-g-C_3N_4, 4% BP-g-C_3N_4, 8%BP-g-C_3N_4, and 12%BP-g-C_3N_4, respectively.

2.3. Evaluation of photocatalytic activity

The degradation of IDM with a concentration of 5 mg/L under VL illumination was monitored to investigate the photocatalytic activity of the prepared BP-g-C_3N_4 samples. In detail, 5 mg of the photocatalyst was added into 50 mL of IDM solution. After that, the mixture solution was magnetically stirred for 30 min in the dark prior to illumination to achieve adsorption-desorption equilibrium. The light source applied was a 300 W Xe lamp, which was equipped with a 400 nm UV cutoff filter (optical power density = 100 mW/cm^2). At the given time intervals, 1 mL of the mixture solution was withdrawn, and filtered by a 0.45 μm filter to remove all the photocatalyst. The residual IDM in the solution was analyzed using a high performance liquid chromatograph (HPLC, Agilent 1260 Infinity II). The IDM was separated using a mobile phase of 70% methanol/30% water containing 0.1% phosphoric acid at 1 mL/min and detected using UV absorbance at 270 nm. The degradation by-products of IDM during the photocatalytic process were analyzed using an Agilent 1260 Infinity II HPLC coupled to a 6470 triple quadrupole mass spectrometer (HPLC-MS).

3. Results and discussion

3.1. Preparation of BP-g-C_3N_4

Construction of the 2D/2D heterostructure photocatalysts by the LPE strategy is favorable for the diffusion and separation of the photogenerated charge carriers, thanks to the intimate "face to face" contact between the layers [Low et al., 2014]. The successful synthesis of the ideal BP-g-C_3N_4 photocatalyst relies greatly on the suitable exfoliation medium. Theoretically, efficient exfoliation can be achieved when the surface energy of the solvent matches with that of the material, because the enthalpy of the mixed system is minimized according to the equation of $\Delta H_{mix}/V_{mix} \approx 2(\delta_G - \delta_{sol})^2\varphi/T_{bulk}$ (ΔH, V_{mix}, δ, φ, and T_{bulk} are the enthalpy of mixing, volume of the dispersion, square root of the component surface energy, nanosheet volume fraction, and average thickness of the nanosheet, respectively) [Hernandez et al., 2008].

The literature results demonstrate that the neighboring BP layers have a surface energy of 58 mJ/m^2, while for g-C_3N_4 it is 70 mJ/m^2 [Mu and Si, 2015; Yang et al., 2013]. It is worth mentioning here that Zhang et al. report a calculated value of 115 mJ/m^2 for the surface energy of g-C_3N_4 [Zhang et al., 2013a]. This implies the possibility for g-C_3N_4 to be efficiently exfoliated in the solvent with a surface energy of >70 mJ/m^2, which is experimentally evidenced by the fact that the efficient solvents for g-C_3N_4 exfoliation display surface energies in the range of 65–85 mJ/m^2 [Ayan-Varela et al., 2015]. Thus, logic dictates that the optimal medium for efficient exfoliation of both g-C_3N_4 and BP should have a surface energy with a specific value in the range of 58–85 mJ/m^2. However, one pure solvent with a surface energy close to that specific value may be rare, or simply not available. It is noticed that ethanol with a relatively low surface energy of 52 mJ/m^2, can be dissolved in water (surface energy = 102 mJ/m^2) in any proportion to form a stable binary azeotrope (the surface energy of a solvent is approximately equal to its surface tension plus 30 mJ/m^2) [Vazquez et al., 1995]. Thus, it seems feasible to obtain an azeotrope with a satisfying surface energy for efficient exfoliation of g-C_3N_4 and BP, by facilely tuning the volume ratio between ethanol and water.

Bearing this in mind, the exfoliation efficiency of the ethanol solutions with varying volume ratios for g-C_3N_4 and BP is studied. First, g-C_3N_4 and BP powders are ultrasonically exfoliated in different ethanol solutions, followed by centrifugation to remove non-exfoliated bulk materials. The amount of dispersed g-C_3N_4 and BP nanosheets (reflecting the exfoliation efficiency of the medium) is estimated by measuring the optical absorbance at 660 nm according to the Lambert-Beer law of $A/l = \alpha C$, where A/l, α, and C are the absorbance per length, extinction coefficient, and concentration, respectively [Coleman et al., 2011]. As expected, water, which is known as a successful medium for the production of g-C_3N_4 nanosheets, exhibits further enhancement in the efficiency after the addition of ethanol (Fig. 1a) [Zhang et al., 2013a]. The best medium is determined to be a 40% ethanol solution (surface energy = 60.16 mJ/m^2 at 25 °C) as the efficiency achieved is obviously greater than that of both pure water and ethanol. In the case of BP, the 50% ethanol solution (surface energy = 57.96 mJ/m^2 at 25 °C) displays the highest performance for the generation of BP nanosheets, which is even better than the performance of the extensively-used NMP, water, and ethanol (Fig. 1b) [Ran et al., 2017; Wang et al., 2015; Zheng et al., 2018]. We note that only a

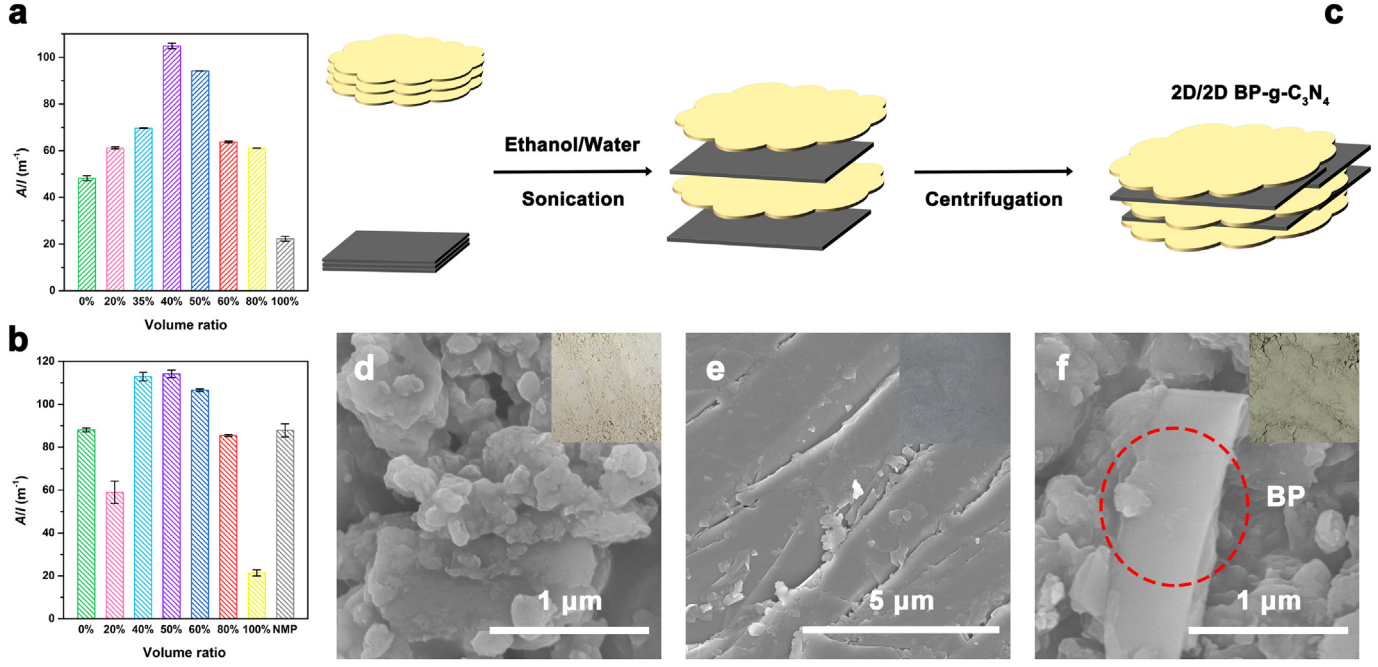

Fig. 1. Concentration of (a) g-C_3N_4 and (b) BP remaining after centrifugation (plotted as A/l) in a mixed solution of ethanol-water with different volume ratios. (c) Schematic illustration for the preparation of BP-g-C_3N_4 photocatalyst by the LEP method. SEM images of (d) g-C_3N_4, (e) BP, and (f) 8%BP-g-C_3N_4.

slight decrease in the efficiency for BP exfoliation can be observed when using 40% ethanol solution as the medium. Thus, 40% ethanol solution is finally selected as the medium for BP-g-C_3N_4 preparation using the LPE method (Fig. 1c), in consideration of its excellent efficiency for the exfoliation of both g-C_3N_4 and BP. It should also be mentioned here that except surface energy, there are other factors affecting the exfoliation efficiency of a medium (e.g., dispersion, polar and H-bonding interactions) [Coleman et al., 2011]. Thus, it is reasonable for the observed phenomenon that water and NMP exhibit a similar efficiency for BP exfoliation.

3.2. Characterization of photocatalyst

First, the morphology of the synthesized photocatalysts is investigated. The scanning electron microscopy (SEM) images of g-C_3N_4, BP, and 8%BP-g-C_3N_4 samples are shown in Fig. 1. Pure g-C_3N_4 exhibits a sheet-like structure with rolling edge and rough external surface (Fig. 1d). BP presents a typical layer-by-layer-stacked structure with sharp edge and a clean and smooth external surface (Fig. 1e). The typical morphology of g-C_3N_4 and BP can also be found in the transmission electron microscopy (TEM) images (Fig. 2a, c). The SEM image for the 8%BP-g-C_3N_4 sample given in Fig. 1f shows the intimate anchoring of BP on the surface of g-C_3N_4, which can also be clearly observed in Fig. 2e. The high-resolution TEM (HRTEM) image given in Fig. 2b shows the amorphous structure of g-C_3N_4. Fig. 2d gives the HRTEM image of BP. The evident lattice fringes with determined *d*-spacing of 0.332 nm (belonging to the (021) plane) indicate the high crystallinity of the as-prepared BP, and this can be further confirmed by the Raman result (Fig. S3) [He et al., 2017]. An observation of the HRTEM image for 8%BP-g-C_3N_4 exhibits the distinct interface established by the close contact between g-C_3N_4 and BP (Fig. 2f). The elemental mappings show the C, N, and P elements are uniformly distributed within the 8% BP-g-C_3N_4 (Fig. 2g), indicating the homogeneous hybridization of g-C_3N_4 and BP, and the presence of these elements is also confirmed by the energy dispersive X-ray spectroscopy (EDS) result (Fig. 2h).

The crystal structure of g-C_3N_4, BP, and 8%BP-g-C_3N_4 samples is investigated by X-ray diffraction (XRD) analysis. The XRD pattern of BP is given in Fig. S4. It is observed that all diffraction peaks of BP are matched well with the standard JCPDS card no. 73–1358. Interestingly, the ratio of (040) to (111) peak is different compared with that of the standard pattern, and this can be explained by the oriented {010} facets in the BP layers [Dong et al., 2015; Zhu et al., 2017]. Pure g-C_3N_4 shows two diffraction peaks (Fig. 3a). The strong peak located at 27.4° originates from the interlayer stacking of conjugated aromatic systems with a distance of 0.325 nm, and it can be indexed as the (002) peak [Wang et al., 2018a]. The weak (100) peak at 13.1° reflects the interplanar separation with a period of 0.675 nm [Wang et al., 2019]. The diffraction peaks related to both g-C_3N_4 and BP are clearly observed for all tested BP-g-C_3N_4 samples, suggesting the successful formation of BP-g-C_3N_4 heterostructures. Taking the 8%BP-g-C_3N_4 as an example, it is found that the ratio of (040)/(111) significantly changes to be closer to that of the standard pattern. This indicates the high dispersion of BP in the 8%BP-g-C_3N_4 heterostructure formed in the ethanol solution.

The textural property of g-C_3N_4 and 8%BP-g-C_3N_4 samples is studied. The nitrogen gas adsorption-desorption isotherms of g-C_3N_4 and 8%BP-g-C_3N_4 given in Fig. 3b reveal the type IV isotherms with H3-type hysteresis loops for the tested samples, implying the presence of slit-like pores. In the pore-size distribution curve of g-C_3N_4, two main distributions are observed at around 3.8 and 57 nm (Fig. 3b, inset). The formation of the smaller pores originates from the released CO_2 and NH_3 during the synthesis process, which can serve as soft templates [Dong et al., 2013]. The larger pores are constructed by the close stacking between g-C_3N_4 layers [da Silva et al., 2017]. The pores with a diameter of 3.8 nm still remain after introducing BP to g-C_3N_4 system, while it is found that the width of the larger pores for 8%BP-g-C_3N_4 is reduced to 53 nm, owing to the different space between the stacked g-C_3N_4 and BP nanosheets (Fig. 3b, inset). It is well known that a larger specific surface area of a catalyst always contributes to the enhancement of its photoactivity, due to the increased adsorption of organic molecules and diffusion of by-products [Sun et al., 2020; Yang et al., 2021]. However, the BET surface area of g-C_3N_4 and 8%BP-g-C_3N_4 is determined to be 28.44 and 22.86 m^2/g, respectively (Table S1). This result indicates the higher catalytic activity of 8%BP-g-C_3N_4 is more possibly due to its efficient charge separation and enhanced ROSs production ability, as is discussed in detail below.

The structural information of g-C_3N_4 and 8%BP-g-C_3N_4 is investigated by Fourier transform infrared (FT-IR) spectroscopy

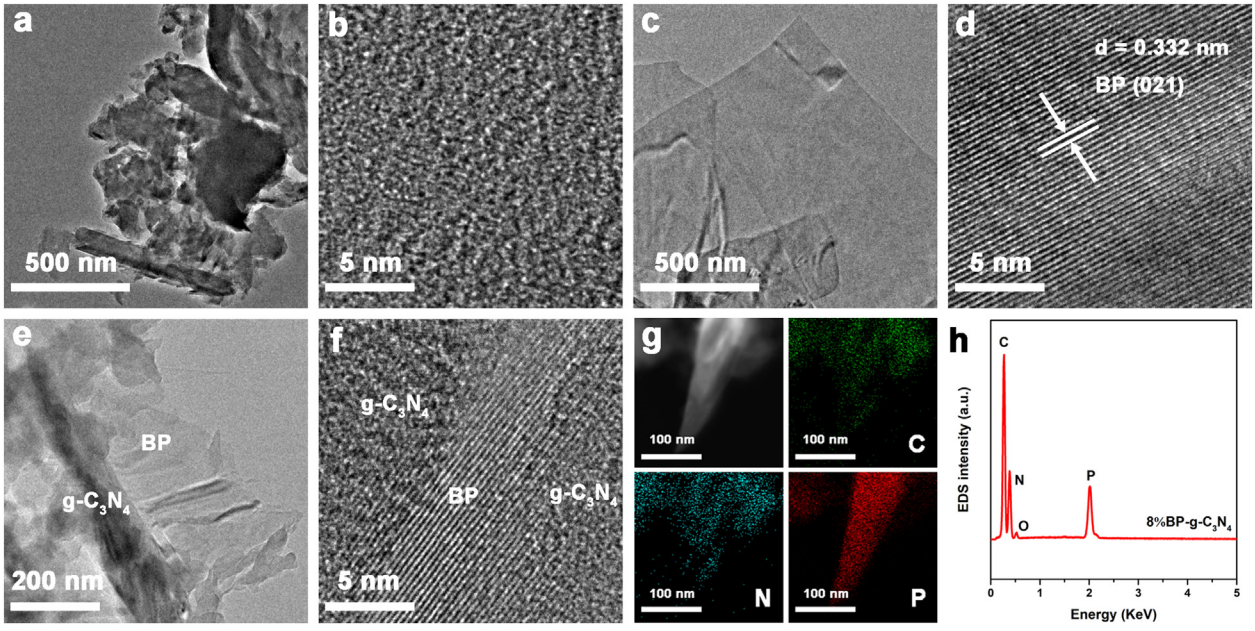

Fig. 2. TEM images of (a) g-C_3N_4, (c) BP, and (e) 8%BP-g-C_3N_4. HRTEM images of (b) g-C_3N_4, (d) BP, and (f) 8%BP-g-C_3N_4. (g) Elemental mappings of 8%BP-g-C_3N_4 for C, N, and P. (h) EDS result of 8%BP-g-C_3N_4.

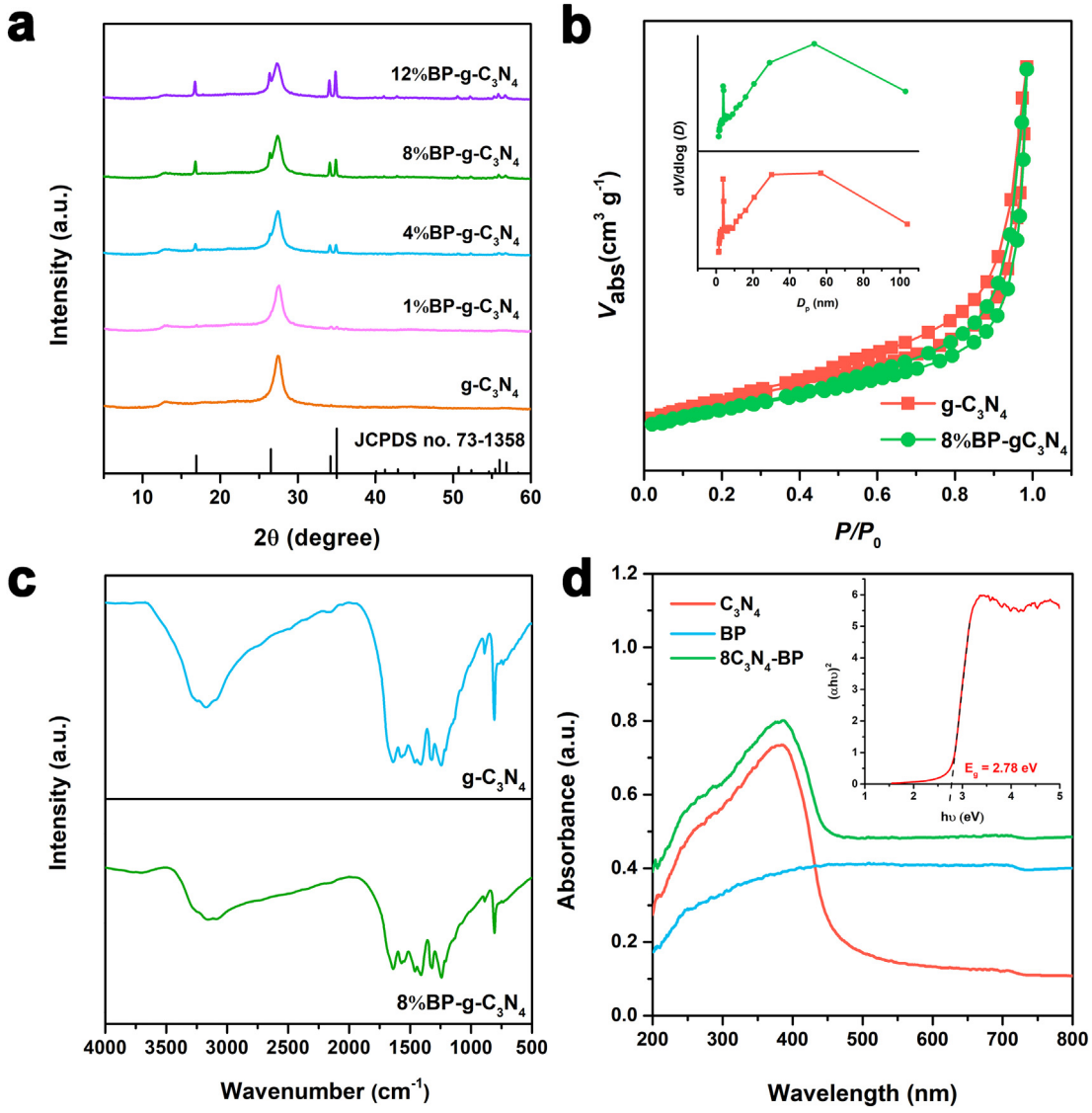

Fig. 3. (a) XRD patterns of g-C_3N_4 and BP-g-C_3N_4 samples. (b) Nitrogen gas adsorption-desorption isotherms of g-C_3N_4 and 8%BP-g-C_3N_4. Inset: pore-size distributions of g-C_3N_4 and 8%BP-g-C_3N_4. (c) FT-IR spectra of g-C_3N_4 and 8%BP-g-C_3N_4. (d) UV–vis diffuse reflectance spectra of g-C_3N_4, BP, and 8%BP-g-C_3N_4. Inset: $(\alpha h\nu)^{1/n}$ versus $h\nu$ curve of g-C_3N_4.

(Fig. 3c). In the case of g-C_3N_4, the peaks observed in the range of 1200 to 1650 cm^{-1} can be attributed to the characteristic of C—N heterocycles [da Silva et al., 2017]. The broad peaks ranging between 3000 and 3300 cm^{-1} are assigned to the stretching vibration of N—H groups [da Silva et al., 2017]. The sharp peak located at 810 cm^{-1} originates from the breathing mode of tri-*s*-triazine units [Ju et al., 2016; Li et al., 2015; Wang et al., 2013]. An obvious change of the positions of these peaks is not observed for 8%BP-g-C_3N_4 sample, indicating that the incorporation of BP with g-C_3N_4 does not result in the destruction of the basic structure of g-C_3N_4.

The optical absorption property of g-C_3N_4, BP, and 8%BP-g-C_3N_4 samples is studied by UV–vis diffuse reflectance spectroscopy. As given in Fig. 3d, BP displays a broad absorption in the tested range of 200–800 nm. As for g-C_3N_4, a typical semiconductor optical absorption with a threshold value of 464 nm is found. After the hybridization of g-C_3N_4 and BP, an intensified light absorption in the entire wavelength range tested, especially in the VL region, is observed. This finding is indicative of the great improvement in the light harvesting ability for g-C_3N_4. The absorption edge of g-C_3N_4 shows a red shift, suggesting the formation of a BP-g-C_3N_4 heterostructure with a narrower bandgap.

The interaction between g-C_3N_4 and BP in the 8%BP-g-C_3N_4 heterostructure is revealed by X-ray photoelectron spectroscopy (XPS) analysis. The XPS survey spectrum given in Fig. S5 demonstrates that 8% BP-g-C_3N_4 is composed of C, N, P, and O elements. The detected O 1s peak for g-C_3N_4 is due probably to inevitable oxidation during the calcination process [Martin et al., 2014]. Fig. 4a shows the high-resolution XPS spectrum of C 1s for g-C_3N_4, two peaks at 284.7 and 288.1 eV can be observed. The first peak is attributed to the carbon-based contaminants used for calibration [He et al., 2020]. The peak located at 288.1 eV is ascribed to the sp^2 bonded C in the aromatic ring (N-C=N) [Zheng et al., 2018]. The N 1s spectrum for g-C_3N_4 can be split into four peaks at 398.6, 399.1, 400.8, and 404.5 eV, respectively (Fig. 4b). These peaks can be attributed to the sp^2 bonded N in C-N=C, the N in $(C)_3$-N groups, the amino functional groups ($C\text{-}NH_x$) caused by the incomplete polymerization, and charging effects, respectively [Cao et al., 2015; Guo et al., 2017]. The P 2p spectrum of BP shows P $2p_{3/2}$, P $2p_{1/2}$, and oxidized phosphorus at 129.9, 130.8, and 133.5 eV, respectively (Fig. 4c) [Zhu et al., 2018]. The binding energies of P 2p for 8%BP-g-C_3N_4 exhibit an obvious shift of 0.75 eV to the direction of lower binding energy, compared with BP. However, owing to the much higher weight ratio of g-C_3N_4 in 8%BP-g-C_3N_4, only a slight shift of 0.05 eV to the higher binding energy is observed for the C 1s peaks of 8%BP-g-C_3N_4, compared with that of g-C_3N_4. These results can be explained by the close van der Waals interaction between the contacted g-C_3N_4 and BP

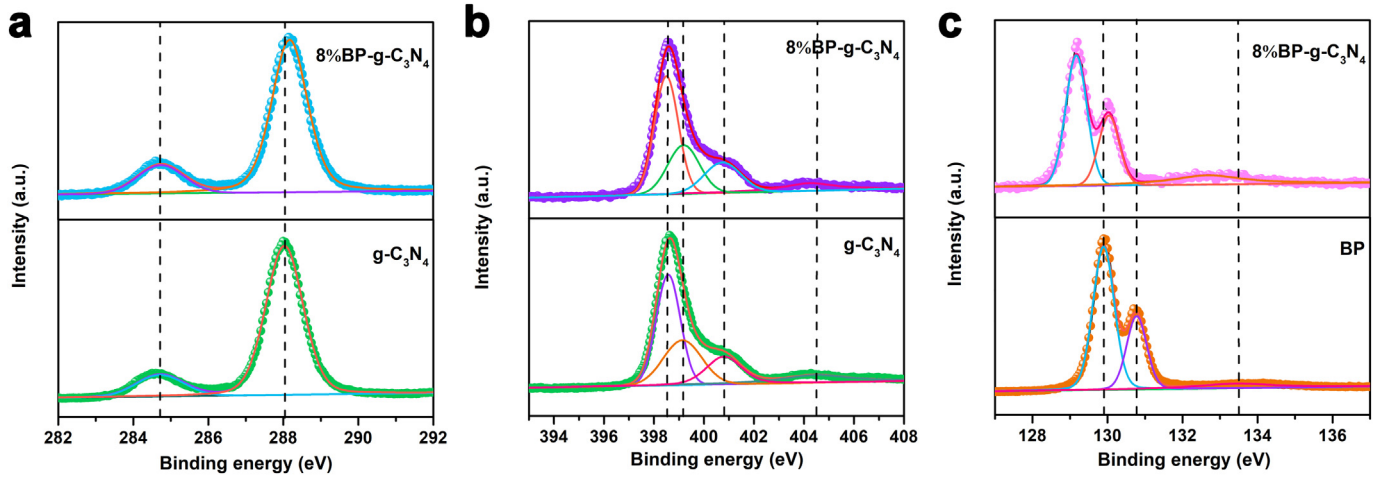

Fig. 4. XPS spectra of (a) C 1s and (b) N 1s for g-C_3N_4 and 8%BP-g-C_3N_4. XPS spectra of (c) P 2p for BP and 8%BP-g-C_3N_4.

layers, as the electron will transfer from the higher Fermi energy level (g-C_3N_4) to the lower Fermi energy level (BP) to achieve an equilibration for the system when the BP-g-C_3N_4 heterostructure is successfully constructed [Zhang et al., 2013b].

3.3. Photocatalytic IDM removal efficiency

The photocatalytic activity of the as-prepared g-C_3N_4, BP, and BP-g-C_3N_4 samples is evaluated by testing the decomposition of IDM under VL illumination. First, the adsorption behavior of the representative g-C_3N_4 and 8%BP-g-C_3N_4 samples is studied. As shown in Fig. S6, the saturation adsorption of the photocatalysts to IDM can be achieved after stirring the mixed suspension for 30 min prior to irradiation, and the adsorption capacity of g-C_3N_4 and 8%BP-g-C_3N_4 toward IDM is 2.6% and 2.3%, respectively. In the direct photolysis test, the concentration of IDM remains almost unchanged within 30 min, indicating the photochemical stability of IDM (Fig. S7). As can be seen in Fig. 5a, BP alone shows a negligible photocatalytic activity, as only 5.2% IDM is degraded within 30 min of VL illumination. However, BP can serve as a powerful cocatalyst for g-C_3N_4 materials to accelerate the decomposition rate of IDM, as confirmed by the boosted activity of the BP-g-C_3N_4 photocatalysts in comparison of bare g-C_3N_4, regardless of the BP loading amounts. The best photocatalytic activity is achieved by the 8%BP-g-C_3N_4 photocatalyst, as 67.1% IDM is degraded within only 10 min, while only 42% IDM is degraded using bare g-C_3N_4. By prolonging the reaction time to 30 min, the removal efficiency for IDM is 99.2% for 8%BP-g-C_3N_4. It is worth mentioning that for bare g-C_3N_4, it requires 80 min to reach a removal efficiency of >99% (Fig. S8). The apparent rate constant for IDM removal over 8%BP-g-C_3N_4 (0.16 min^{-1}) is determined to be ~2.81 times higher than that of g-C_3N_4 (0.057 min^{-1}), as shown in Fig. S9. This constitutes a statistically significant difference in rate constants. It is also found that the photoactivity of 8%BP-g-C_3N_4 can be dramatically enhanced by adjusting the solution pH (~100% degradation efficiency for IDM can be achieved within 10 min at pH = 4), arising from the improvement of the adsorption capacity (Fig. S10). Compared to 8%BP-g-C_3N_4, the lower activity of 1%BP-g-C_3N_4 and 4%BP-g-C_3N_4 can be explained by the insufficient loading of BP. Taking 1%BP-g-C_3N_4 as an example, from its SEM as well as elemental mapping images (Fig. S11), BP can hardly be found on the surface of g-C_3N_4. This suggests that only a part of g-C_3N_4 can construct a heterostructure with BP, thus hampering the photocatalytic activity. In contrast, the decay of activity of 12%BP-g-C_3N_4 is due to the shielding of light by excessive BP (Fig. S12), since the role of BP in the current photocatalytic system is to work as a cocatalyst to catalyze the generation of ROSs, rather than to act as a light absorber like g-C_3N_4, as is discussed in detail below.

As shown in Fig. 5b and c, 8%BP-g-C_3N_4 outperforms the extensively-used P25 TiO_2 (20 nm) in IDM removal, under both VL and real-sunlight irradiation. Using natural sunlight as the light source (16 August 2020, Northeast Normal University, average light intensity: 89.2 mW/cm^2), the determined apparent rate constant for IDM removal over 8%BP-g-C_3N_4 is ~11 times higher than that of P25 TiO_2 (Fig. S13). Also, the catalytic activity of 8%BP-g-C_3N_4 is comparable to that of the best photocatalysts developed previously (Fig. 5e). Under VL illumination, 8%BP-g-C_3N_4 exhibits a much greater decomposition rate for IDM compared to some recently-reported photocatalysts, such as carbon dots/$BiPO_4$, C and O doped g-C_3N_4, and N-doped carbon dots/g-C_3N_4, but only consumes 1/10–1/4 of the catalyst. As for the O-containing carbon quantum dots/g-C_3N_4 photocatalyst that shows a faster IDM degradation rate than 8%BP-g-C_3N_4 (18 min for complete removal of IDM), we re-conduct the photocatalytic activity test using an equal mass of 8% BP-g-C_3N_4 (0.5 mg/mL), and observe that the IDM can be almost completely degraded within only 10 min, with a rate constant of 0.54 min^{-1} (Fig. S14).

A comparison of the photocatalytic activity of the 8%BP-g-C_3N_4 samples prepared in different exfoliation mediums is given in Fig. 5f. The 8%BP-g-C_3N_4 synthesized in 40% ethanol solution shows the highest rate constant for IDM removal among various counterparts prepared in the other media. Owing to the poor efficiency of ethanol for the exfoliation of both g-C_3N_4 and BP, despite after a lengthy ultrasonication duration of 8 h, the 8%BP-g-C_3N_4 prepared in ethanol shows even lower activity than bare g-C_3N_4. The 8%BP-g-C_3N_4 photocatalyst is also prepared via a mechanical mixing process, which shows the lowest rate for IDM degradation. This suggests the photocatalytic activity of 8%BP-g-C_3N_4 can be greatly affected by the contact between g-C_3N_4 and BP layers. From all the above-mentioned results, we can conclude that the exfoliation medium plays an important role in the successful synthesis of high-efficiency BP-g-C_3N_4 photocatalysts, as the improvement of catalytic performance is the result of the interfacial interaction between g-C_3N_4 and BP based on an efficient exfoliation.

The stability as well as reusability of 8%BP-g-C_3N_4 are examined by repeating the photocatalytic IDM decomposition test for four times. Before the next cycle, the 8%BP-g-C_3N_4 catalyst is collected by a centrifugation process, and subsequently resuspended in a freshly prepared IDM solution, without any additional pretreatment between the runs. As can be seen in Fig. 5g, 8%BP-g-C_3N_4 exhibits excellent photocatalytic activity after 4 recycles, as 95.9% IDM can still be degraded within 30 min. The XRD and FT-IR results of the recycled sample are shown in Fig. S15. The crystal phase and chemical structures of the used 8%BP-g-C_3N_4 are retained after the photocatalytic reaction. In addition, the XPS result of 8%BP-g-C_3N_4 after photocatalytic reaction shows that only a small part of BP is oxidized to P_xO_y (Fig. S15). These

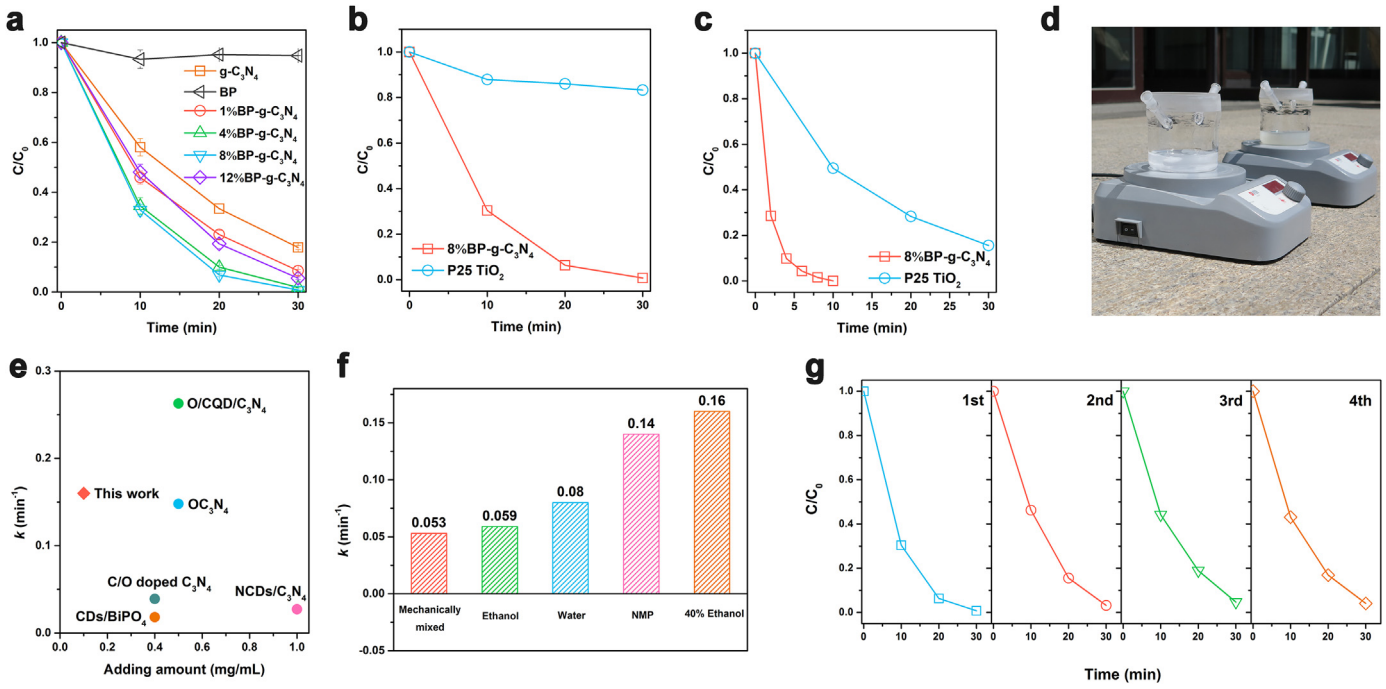

Fig. 5. (a) Photocatalytic activity of g-C_3N_4, BP, and BP-g-C_3N_4 samples toward IDM degradation under VL irradiation. Photocatalytic performance comparison between 8%BP-g-C_3N_4 and P25 TiO_2 under (b) VL and (c) real-sunlight irradiation. (d) Experimental set-up for photocatalytic reactions of 8%BP-g-C_3N_4 and P25 TiO_2 under real-sunlight irradiation. (e) Photocatalytic performance comparison of 8%BP-g-C_3N_4 with the literature values of other photocatalysts. The plot gives the apparent rate constant of IDM removal with respect to catalyst consumption: (1) O/CQD/g-C_3N_4 (Wang et al., 2019), (2) CDs/$BiPO_4$ (Zhang et al., 2018b), (3) NCDs/g-C_3N_4 (Wang et al., 2017), (4) C/O doped g-C_3N_4 (Zheng et al., 2020b), (5) Og-C_3N_4 (Zhang et al., 2018a). Details of the experimental conditions, including initial IDM concentration, light source, catalyst dosage are given in Table S2. (f) Photocatalytic performance comparison of 8%BP-g-C_3N_4 prepared by LPE method using different exfoliation mediums. (g) Cycling runs for the photocatalytic decomposition of IDM using 8%BP-g-C_3N_4 under VL irradiation.

results firmly confirm the feasibility of 8%BP-g-C_3N_4 to be used as a recyclable catalyst for photocatalytic removal of PPCPs. The slight decay in the removal efficiency is due probably to the ineluctable loss of material during the multicycle tests.

3.4. The mechanism for enhanced photocatalytic activity of 8%BP-g-C_3N_4

Normally, the photoactivity of a photocatalyst is largely governed by the efficiency of two key catalytic processes, namely: (1) the separation and transfer of the photo-generated charge carriers to the surface of catalyst; and (2) the catalytic redox reactions on the surface for ROSs production. To obtain the detailed insights into the first property, the semiconductor property of g-C_3N_4 and BP nanosheets is determined, as the band structure is one of the most crucial factors determining the charge-carrier separation efficiency. First, the bandgap energy (E_g) of the g-C_3N_4 nanosheet is estimated according to the plot of $(\alpha h\nu)^{1/n}$ versus $h\nu$, where α, h, and ν are the absorption coefficient, Planck constant, and light frequency, respectively [Zheng et al., 2020b]. In this equation, n is equal to 1/2 due to the direct bandgap of g-C_3N_4 [He et al., 2020]. Accordingly, the E_g value of g-C_3N_4 is determined to be 2.78 eV (Fig. 3d, inset). The E_g value of the BP nanosheet is estimated by the UV–vis absorption spectrum shown in Fig. S16. The absorption edge gives 739 nm for the BP nanosheet, corresponding to the E_g value of 1.68 eV. Subsequently, the Mott-Schottky test is performed, showing the n-type semiconductor nature for g-C_3N_4 and BP nanosheets (Fig. S17). That is to say, the flat band potential of g-C_3N_4 and BP nanosheets acquired from the Mott-Schottky results can roughly estimate their conduction band (CB) values. Thus, the CB value of g-C_3N_4 and BP nanosheets is determined to be −1.13 and − 1.04 V versus Ag/AgCl, corresponding to −0.52 and − 0.43 V versus NHE, respectively. The valence band (VB) potential of g-C_3N_4 and BP nanosheets is then calculated to be 2.26 and 1.25 V versus NHE, respectively. According to the band structure of g-C_3N_4 and BP, a typical type I heterostructure is established.

It is known that the successful establishment of a type I heterojunction can lead to efficient separation of the charge carriers at the contacted interface [Fang et al., 2011]. In the case of the 8%BP-g-C_3N_4 heterostructure, although both the photo-induced charge carriers will transfer from g-C_3N_4 to BP, the different transfer rate of e^- and h^+ can result in charge carrier separation inside the heterostructure [Wang et al., 2018b]. To verify this, various photoelectrochemical experiments are conducted. The transient photo-current (TPC) response curves for g-C_3N_4 and 8%BP-g-C_3N_4 are given in Fig. 6a. The steady and reproducible TPC responses for the tested g-C_3N_4 and 8%BP-g-C_3N_4 working electrodes are observed during the successive on/off cycles of Xe light irradiation. The TPC response for the 8%BP-g-C_3N_4 electrode is obviously higher than that of the g-C_3N_4 electrode, indicating enhanced separation as well as a prolonged lifetime of the photo-excited charge carriers after the combination of g-C_3N_4 and BP. One should note that BP is proven to be inefficient in the production of photo-induced charge carriers [Xiong et al., 2020]. That is to say, the role of BP is to inhibit the recombination of e^--h^+ pairs, rather than to act as a light absorber like g-C_3N_4 to produce charge carriers. This can also be confirmed by the experimental evidence reported by Ran et al., that the CdS/BP hybrid photocatalyst displays negligible photoactivity when using a light filter to cut off the incident light with a wavelength shorter than the absorption edge of CdS [Ran et al., 2017].

The effect of BP loading on the diffusion and transfer of the charge carriers is also studied by electrochemical impedance spectroscopy (EIS) measurement (Fig. 6b). Under VL illumination, according to a smaller arc radius given by 8%BP-g-C_3N_4, a lower resistance for charge migration on its surface is found. This suggests enhanced transfer efficiency for charge carriers in 8%BP-g-C_3N_4, which can be further confirmed by photoluminescence (PL) investigation. Fig. 6c shows the steady-state PL spectra for g-C_3N_4 and 8%BP-g-C_3N_4. A decrease in the PL intensity for 8%BP-g-C_3N_4 compared to that of C_3N_4 implies the suppressed recombination and improved separation efficiency of the charge carriers after incorporating of g-C_3N_4 with BP. The results from

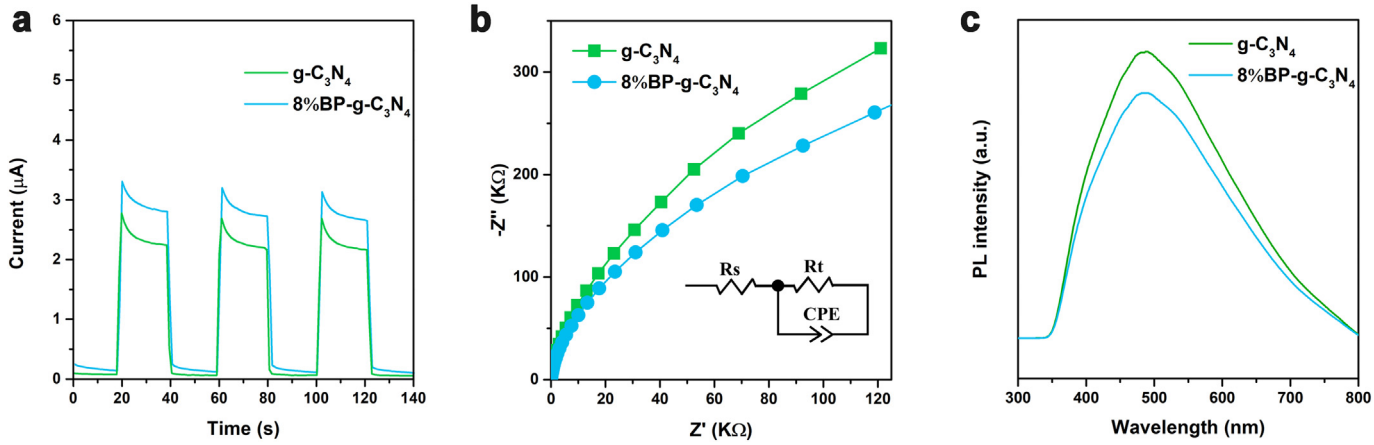

Fig. 6. (a) TPC responses, (b) EIS Nyquist plots, and (c) PL spectra of g-C_3N_4 and 8%BP-g-C_3N_4.

TPC, EIS, and PL measurements firmly confirm that the introduction of BP can effectively elongate the charge carriers' lifetime and facilitate their transportation.

Generally, efficient separation and transfer of the photo-generated charge carriers is favorable for the enhancement of the activity of a photocatalyst, benefiting from the sufficient time provided for the e^--h^+ pairs to participate into the oxygen-reduction reaction for ROSs production. To verify this, the ROSs generating ability of g-C_3N_4 and 8% BP-g-C_3N_4 is evaluated by the probe-molecule-involved specific reactions. It is known that nitroblue tetrazolium (NBT) can specifically react with $\bullet O_2^-$ to produce precipitates, showing a decay for the absorption intensity at around 259 nm. As shown in Fig. S18, a greater consumption of NBT is observed for 8%BP-g-C_3N_4 compared with that of g-C_3N_4, indicating the boosted $\bullet O_2^-$ photo-generating ability after the modification with BP. The concentration of steady-state $\bullet O_2^-$ is calculated to be 1.09×10^{-9} and 2.69×10^{-9} M, for the g-C_3N_4 and 8%BP-g-C_3N_4 systems, respectively (Fig. 7a). Furfuryl alcohol (FFA) is a well-known indicator for $^1O_2$ generation, and its decay is monitored after the exposure of the catalyst-containing system to VL irradiation. The measurement is conducted in the presence of isopropanol (1 mM) considering the second-order reaction rate constant of 1.5×10^{10} M^{-1} s^{-1} between •OH and FFA [Mostafa and Rosario-Ortiz, 2013]. The stronger efficiency of 8%BP-g-C_3N_4 in $^1O_2$ production is confirmed to be due to its faster decomposition of FFA compared to g-C_3N_4 (Fig. S19), and the corresponding concentration of steady-state $^1O_2$ is determined to be 9.34×10^{-13} and 1.01×10^{-12} M for the g-C_3N_4 and 8%BP-g-C_3N_4 systems, respectively (Fig. 7b).

Electron spin resonance (ESR) spectroscopy has been considered as the most direct evidence for the identification of the ROSs generated. To verify the presence and production of $\bullet O_2^-$, •OH, and $^1O_2$ in g-C_3N_4 and 8%BP-g-C_3N_4 systems, two trapping agents, 5,5-dimethyl-1-pyrroline-*N*-oxide (DMPO) and 2,2,6,6-tetramethylpiperidine (TEMP), are employed to detect the reaction systems using ESR technology. As displayed in Fig. 7c and d, the weak characteristic signals for DMPO-$\bullet O_2^-$ and DMPO-•OH adducts are identified in the g-C_3N_4 system, indicating the generation of $\bullet O_2^-$ and •OH at small amounts. However, 8%BP-g-C_3N_4 gives remarkably stronger signals related to DMPO-$\bullet O_2^-$ and DMPO-•OH adducts, suggesting that more abundant $\bullet O_2^-$ and •OH radicals can be produced after the combination of g-C_3N_4 with BP. In addition, $^1O_2$ generation by g-C_3N_4 and 8%BP-g-C_3N_4 is confirmed by the observation of the typical ESR signals that are characteristic for 2,2,6,6-tetramethylpiperidine-N-oxyl (TEMPO), and also the higher $^1O_2$ generation ability of 8%BP-g-C_3N_4 is identified (Fig. 7e). No ESR signal can be found in the dark, indicating that the reaction related to the generation of ROSs is based on the photo-excited charge carriers in the catalysts (Fig. S20).

Taking together all the above results and analyses, it can be inferred that the enhanced photocatalytic performance of 8%BP-g-C_3N_4 is attributed to the following reasons. On the one hand, the coupling of g-C_3N_4 and BP can suppress the recombination of the photo-generated e^--h^+ pairs efficiently, which is favorable for the catalytic redox reactions that follow. This can be explained by the successful construction of type I heterojunction at the contacted g-C_3N_4 and BP interfaces, where efficient charge carrier separation occurs arising from the difference in the migration rate of e^- and h^+ from g-C_3N_4 to BP [Wang et al., 2018b]. On the other hand, the prolonged lifetime of the charge carriers gives them sufficient time to participate into the catalytic oxygen-reduction process, favoring the generation of more abundant ROSs in the 8%BP-g-C_3N_4 system for IDM removal.

3.5. Photocatalytic mechanism

The contribution of the generated ROSs for the decomposition of IDM is investigated by the comparison of the photocatalytic activity of 8%BP-g-C_3N_4 with and without the presence of different kinds of scavengers. The concentration applied for the used scavengers is optimized before conducting the experiments to ensure their maximum quenching effect. As shown in Fig. 7f, the critical role of $\bullet O_2^-$ is confirmed by the residual of 66.8% IDM in the presence of TEMPOL. In addition, the heavy involvement of $^1O_2$ is affirmed by the obvious decay in the photocatalytic efficiency after adding L-histidine into the reaction system. With the addition of sodium oxalate, a slight decrease in the photocatalytic efficiency is observed, revealing the moderate role of the photo-generated h^+ for IDM decomposition. Although •OH has been considered as the most active oxidant for the degradation of organic pollutants, it only exhibits a minor contribution in removing IDM, which is evidenced by the almost unchanged performance of 8%BP-g-C_3N_4 after adding isopropanol. Similar contribution of $\bullet O_2^-$, $^1O_2$, •OH, and photo-generated h^+ toward the IDM decomposition is also observed in the g-C_3N_4 system, as shown in Fig. S21.

Owing to the successful establishment of the type I heterostructure of BP-g-C_3N_4, the photo-induced e^- and h^+ in g-C_3N_4 will transfer to BP. It is known that the redox potential for $O_2/\bullet O_2^-$ is −0.33 V versus NHE, thus it is feasible for the e^- in the CB of BP to reduce the absorbed O_2 to generate $\bullet O_2^-$, as the CB potential of BP is sufficiently negative [Li et al., 2019; Zheng et al., 2018]. The $\bullet O_2^-$ can then be oxidized by the h^+ in the VB of BP for $^1O_2$ generation [Liu et al., 2016]. Interestingly, the radical quenching results demonstrate the greater inhibitory effect of L-histidine than that of sodium oxalate, and this can be explained by the enhanced separation efficiency of the charge carriers after quenching the photo-induced h^+. It should be noted that the direct oxidation of OH^-/H_2O to produce •OH is thermodynamically unavailable, because the VB potential of BP is not sufficiently positive ($OH^-/\bullet OH = 2.40$ V versus NHE, $H_2O/\bullet OH = 2.72$ V versus NHE) [He et al., 2021; Jiang et al., 2018]. Thus, the observed •OH is likely to be generated via a reduction

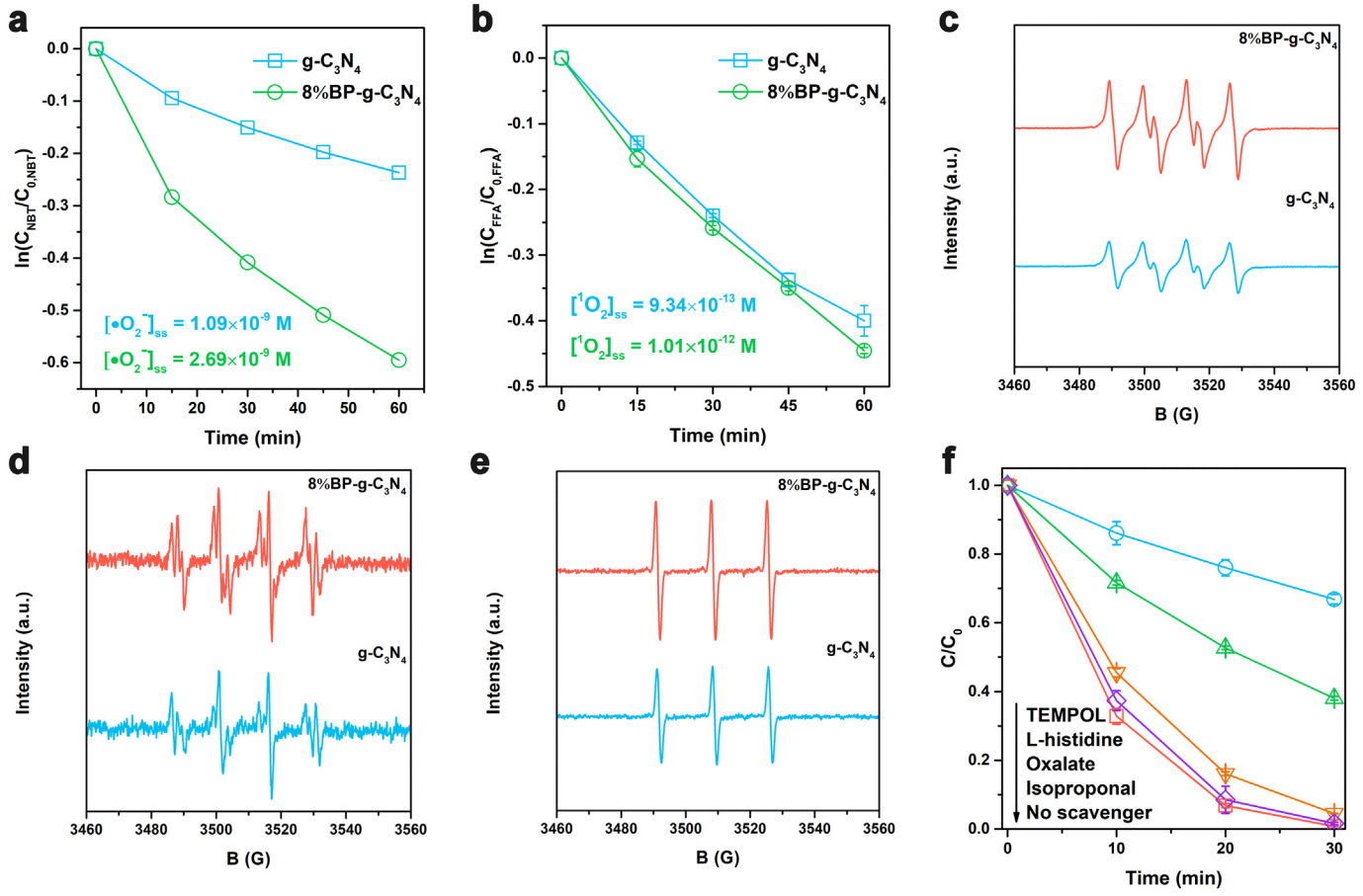

Fig. 7. Steady-state concentration of (a) $•O_2^-$, (b) $^1O_2$ in g-C_3N_4 and 8%BP-g-C_3N_4 reaction systems. ESR spectra of g-C_3N_4 and 8%BP-g-C_3N_4 with VL irradiation for the detection of (c) $•O_2^-$, (d) •OH, and (e) $^1O_2$. (f) Photocatalytic efficiency of 8%BP-g-C_3N_4 toward IDM removal in the presence of different scavengers.

reaction, that $•O_2^-$ can be reduced by accepting a photo-excited e^- to produce H_2O_2, which can be further activated to generate •OH [Nosaka and Nosaka, 2017]. The migration of the charge carriers from g-C_3N_4 to BP will result in the inevitable deterioration of their redox capacity. However, efficient separation of the photo-generated e^--h^+ pairs is the more important factor determining the ROSs production amount, thus dominating the photocatalytic activity. Based on the above analysis, a catalytic reaction mechanism of 8%BP-g-C_3N_4 catalyst is shown in Fig. 8.

A theoretical calculation of the frontier electron densities (FED) for IDM is carried out to forecast the reaction sites for ROSs attack (Fig. 9a-c). Theoretically, the positions with larger $2FED^2_{HOMO}$ values are more vulnerable to be attacked by oxidants; while the positions with larger $FED^2_{HOMO} + FED^2_{LUMO}$ values are more susceptible for addition of ROSs (Table S3) [Sun et al., 2019]. Accordingly, the C2, C4, C6, C7, and C9 positions are likely to be attacked by oxidants, while the hydroxylation of IDM probably occurs at the C7, C9, C17 and C24 positions. By combining the results of HPLC-MS (Fig. S23), the potential IDM decomposition pathways in the 8%BP-g-C_3N_4 photocatalytic system are proposed, as shown in Fig. 9d. First, the amide bond is attacked by $•O_2^-$ with a nucleophilic reaction, giving rise to the cleavage of the C17-N1 bond to form byproduct 1a [Zhang et al., 2018b]. Meanwhile, $^1O_2$-addition at C2 and C3 leads to the destruction of the C2=C3 bond to generate byproduct 1c, which can be further oxidized to produce byproduct 1d. Also, during the cleavage of amide bond, $^1O_2$-substitution can take place at C9 and hydroxylation can occur at C2 and C11, leading to the production of byproduct 2b. Byproduct 2b can undergo ROSs initiated oxidation, leading to the formation of byproducts 2c and 2d. It should be noted that the C9 position also has a high $FED^2_{HOMO} + FED^2_{LUMO}$ value, suggesting the possibility for the cleavage of the C9-N1 bond through a $^1O_2$-addition pathway. The corresponding byproduct can easily undergo further oxidation by ROSs to form byproduct 2a. In addition, the C17-C18 bond can be cleaved as a result of $^1O_2$-addition reaction to form byproducts 3a and 3b, in consideration of the high $FED^2_{HOMO} + FED^2_{LUMO}$ value of the C17 atom. Byproduct 3b can be further oxidized into byproducts 3c and 3d. All of these byproducts can be further oxidized by ROSs generated during the photocatalytic process, finally leading to mineralization.

3.6. Toxicity estimation

In consideration of the possibility that the generated byproducts during the decomposition process may be more toxic than IDM itself, the acute and chronic toxicity of the intermediates at three trophic levels is calculated based on quantitative structure activity relationships (QSARs) using the ECOSAR program. In the case of IDM, the acute toxicity (EC_{50} for green algae, and LC_{50} for fish and daphnia) is estimated as 2.92, 3.60, and 2.72 mg/L, for green algae, fish and daphnia, respectively (Table S4). According to the system established by the Globally Harmonized System of Classification and Labeling of Chemicals, IDM is classified as toxic at all three trophic levels [Sui et al., 2017]. The chronic toxicity value (ChV) of IDM is calculated to be 1.59, 0.33, and 0.37 mg/L, toward green algae, fish and daphnia, respectively, indicating that IDM is chronically toxic to all three selected aquatic organisms.

From the viewpoint of both acute and chronic toxicity, the predicted toxicity of all the identified intermediates is lower than that of IDM itself, and most byproducts can be classified as non-harmful (LC_{50}, EC_{50}, ChV > 100 mg/L) toward the three tested organisms. As given in

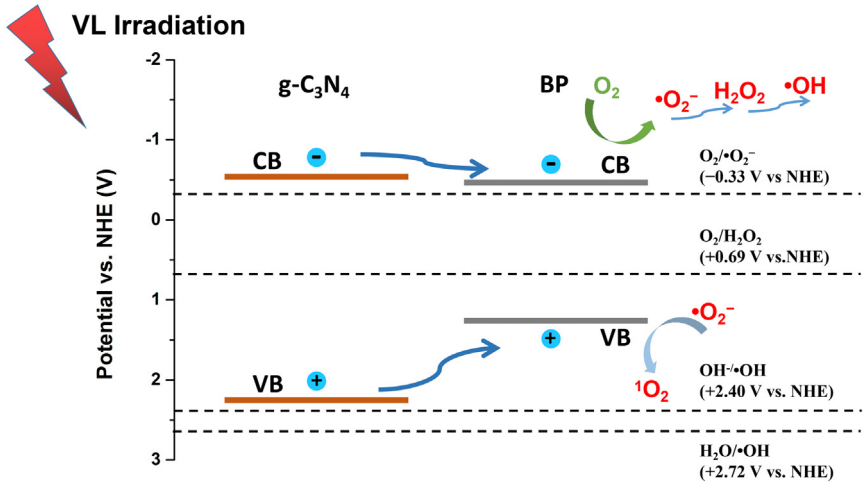

Fig. 8. Proposed photocatalytic reaction mechanism of 8%BP-g-C_3N_4.

Fig. S24, only four intermediates are considered to be harmful or toxic, and most of the levels of toxicity of the intermediates are determined to be at least one order of magnitude lower than that of IDM. Thus, it is quite confirmative that 8%BP-g-C_3N_4 can be applied as a suitable photocatalyst for "green" elimination of IDM from water.

3.7. Feasibility for practical water treatment applications

To evaluate the environmental application of 8%BP-g-C_3N_4, photocatalytic decomposition of IDM is conducted in the presence of different natural water constituents. As shown in Fig. 10a, obvious effect of Cl^-, SO_4^{2-}, and Ca^{2+} on the removal efficiency of IDM is not observed. However, the addition of HCO_3^- and NO_3^- clearly inhibits the decomposition of IDM. The restraint of HCO_3^- may be due to its scavenging ability for h^+ and •OH [Hu et al., 2004]. While the inhibition of NO_3^- can be explained by the decreased active site number on the surface of 8%BP-g-C_3N_4 [Zhang et al., 2005]. The effect of fulvic acid (FA) on IDM degradation is also investigated. It is found that the presence of FA significantly improves the decomposition efficiency of IDM, and this may be attributed to the enhanced production amount of $•O_2^-$. It is reported that $•O_2^-$ can also be generated via the reaction of absorbed O_2 with the e^- transferred from FA to the catalyst surface [Shang et al., 2017].

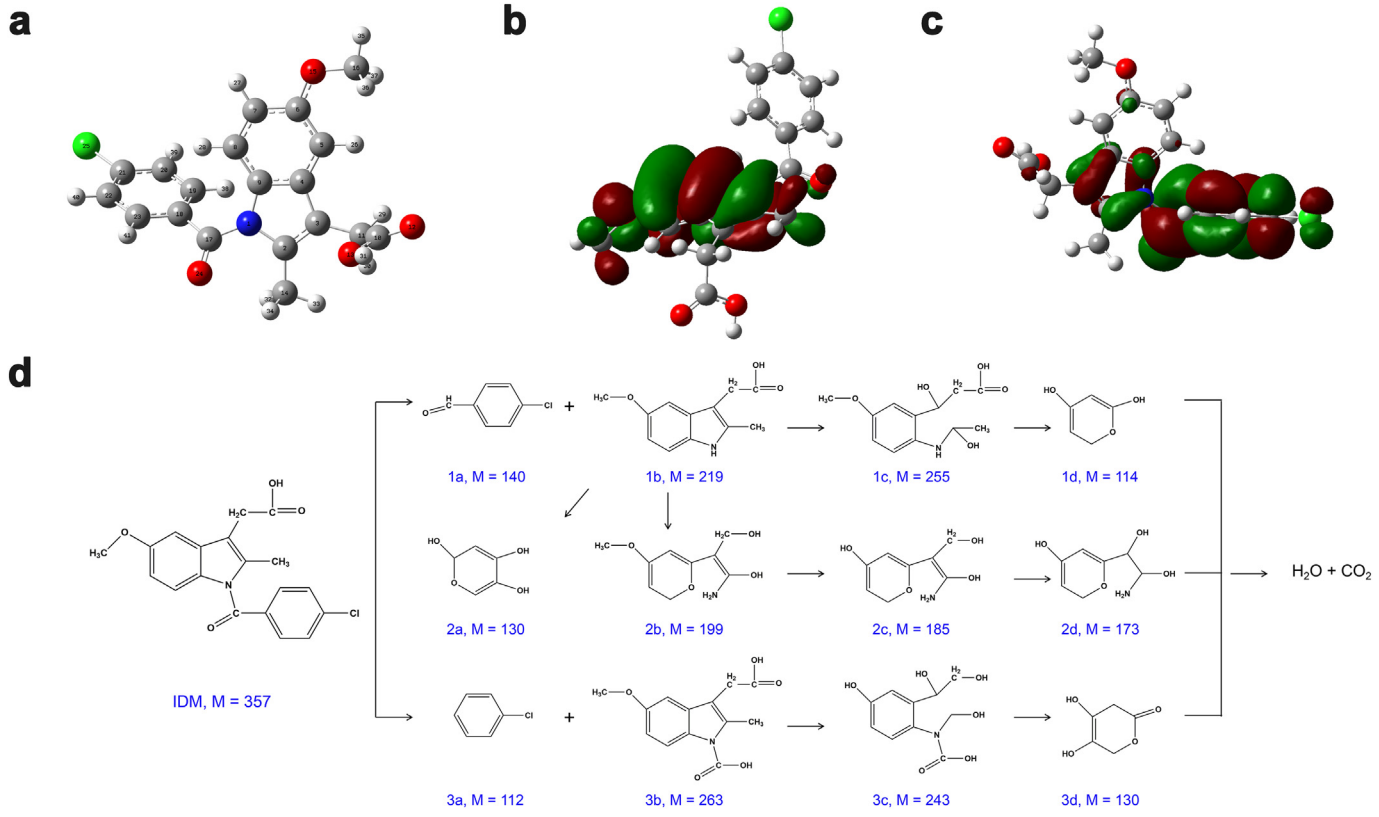

Fig. 9. (a) The atomic numbering of IDM: the gray, dark gray, red, blue and green spheres are H, C, O, N, and Cl atoms, respectively. The (b) HOMO and (c) LUMO of IDM calculated by using Gaussian 09 program at the B3LYP/6–31 + g(d, p) level. (d) Photocatalytic degradation pathways of IDM.

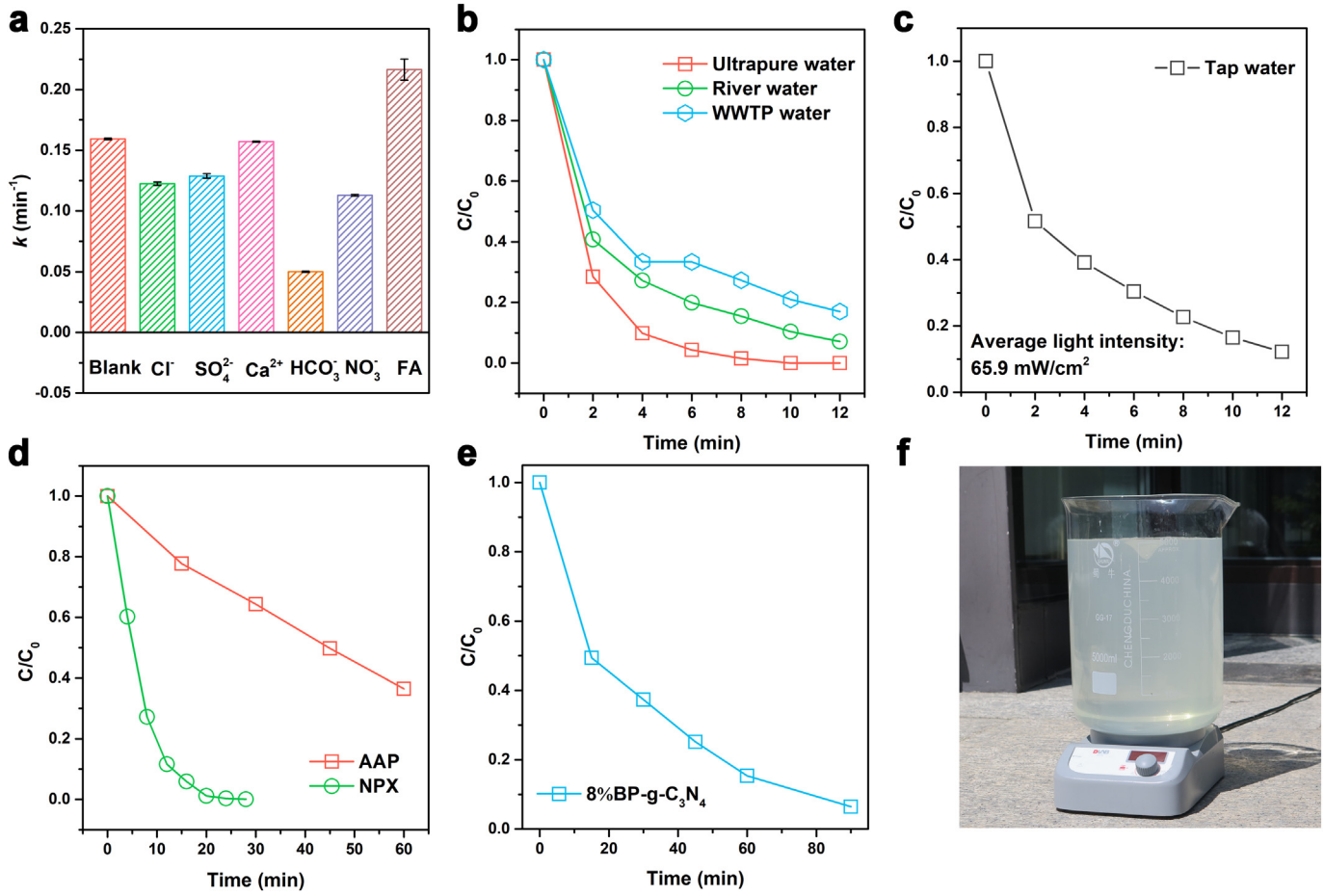

Fig. 10. (a) Kinetic rate constant of IDM over different ions (5 mM) and FA (5 mg/L). (b) Photocatalytic activity of 8%BP-g-C_3N_4 toward IDM degradation in different water matrices under natural sunlight. (c) Photocatalytic activity of 8%BP-g-C_3N_4 toward IDM degradation in tap water under natural sunlight. (d) Photocatalytic activity of 8%BP-g-C_3N_4 toward NPX and AAP degradation under natural sunlight. (e) Large-scale application demonstration at 5000 mL under natural sunlight (catalyst dosage: 0.01 mg/mL). (f) Experimental set-up for large-scale reaction of 8%BP-g-C_3N_4 under real-sunlight irradiation.

The photocatalytic IDM removal experiment is also conducted in authentic water matrices under real-sunlight irradiation. As shown in Fig. 10b, the inhibition for IDM decomposition in Yitong river water (92.9% removal) and secondarily treated sewage effluent water (83% removal) is observed (September 2020, Northeast Normal University, the timely-monitored light intensity is given in Supporting Information). This observation is reasonable, since the total organic carbon (TOC) value is much higher in these water samples than in the ultrapure water (Table S5). These organic compounds can act as natural scavengers for quenching ROSs. In consideration of the relatively lower amount of organic components in tap water, we deliberately conduct the IDM removal test in tap water on a cloudy day (September 2020, Northeast Normal University, average light intensity: 65.9 mW/cm^2), and observe that 87.8% IDM can be degraded within 12 min of natural sunlight irradiation (Fig. 10c). The above results indicate the practicality of 8%BP-g-C_3N_4 for authentic water treatment applications.

An ideal photocatalyst for practical PPCPs remediation applications is expected to be able to decompose a variety of contaminants. To evaluate this, the photocatalytic removal of two other representative PPCPs pollutants, naproxen (NPX) and acetaminophen (AAP), by the 8%BP-g-C_3N_4 photocatalyst is studied under real-sunlight irradiation (August 2020, Northeast Normal University, the timely-monitored light intensity is given in Supporting Information). As shown in Fig. 10d, a high efficiency of 8%BP-g-C_3N_4 toward the degradation of NPX (28 min for 99.9% degradation rate) and AAP (60 min for 63.5% degradation rate) is also achieved (catalyst dosage: 0.1 mg/mL). The corresponding apparent rate constant for NPX and AAP removal is calculated to be 0.26 and 0.016 min^{-1}, respectively (Fig. S26). The different efficiency for NPX and AAP removal in 8%BP-g-C_3N_4 system may be due to the different adsorption ability of the catalyst toward different pollutants. As can be seen in Fig. S28, that the adsorption-desorption equilibrium between NPX and 8%BP-g-C_3N_4 reaches after stirring the mixture solution for 30 min (adsorption ability: 5.3%), while 8%BP-g-C_3N_4 exhibits negligible absorption capacity toward AAP.

The demonstration of scaled-up application at 5000 mL is then carried out under real-sunlight irradiation (August 2020, Northeast Normal University, the timely-monitored light intensity is given in Supporting Information), the catalyst dosage is 10 times lower than that of laboratory-scale tests (0.01 mg/mL). However, the results show that 93.5% of IDM can still be removed within 90 min (Fig. 10e), indicating 8%BP-g-C_3N_4 has great potential to be used for practical applications. These results indicate the feasibility of 8%BP-g-C_3N_4 to be applied as a low-cost and high-efficiency photocatalyst for real-world water treatment operations.

4. Conclusions

In conclusion, the successful preparation of a low-cost 8%BP-g-C_3N_4 photocatalyst by a newly-developed single-step LPE strategy is demonstrated. The 8%BP-g-C_3N_4 heterostructure exhibits an apparently raised photocatalytic activity toward the decomposition of IDM compared with that of pure g-C_3N_4, with 99.2% removal of IDM within only 30 min of VL irradiation. The combination of g-C_3N_4 and BP successfully facilitates the charge-carrier transfer and separation. This enable the 8%

BP-g-C_3N_4 to generate ROSs efficiently for IDM decomposition. Our work will open up new possibilities not only in the development of purely metal-free photocatalysts for "green" environmental remediation, but also in the simple production of high-performance 2D/2D heterostructures for a variety of photocatalytic applications.

CRediT authorship contribution statement

Dongyang He: Conceptualization, Methodology, Investigation, Writing – original draft. **Dexin Jin:** Investigation. **Fangyuan Cheng:** Formal analysis. **Tingting Zhang:** Formal analysis. **Jiao Qu:** Supervision, Funding acquisition, Writing – review & editing. **Yangjian Zhou:** Investigation. **Xing Yuan:** Resources. **Ya-nan Zhang:** Formal analysis, Funding acquisition. **Willie J.G.M. Peijnenburg:** Writing – review & editing.

Declaration of competing interest

The authors declare that they have no known competing financial interests or personal relationships that could have appeared to influence the work reported in this paper.

Acknowledgements

This work is supported by National Natural Science Foundation of China (42130705, 22176030, 51479005, 41877364, and 41702370) and Jilin Province Science and Technology Development Projects (20200301012RQ).

Appendix A. Supplementary data

Supplementary data to this article can be found online at https://doi.org/10.1016/j.scitotenv.2021.150062.

References

Archer, E., Petrie, B., Kasprzyk-Hordern, B., Wolfaardt, G.M., 2017. The fate of pharmaceuticals and personal care products (PPCPs), endocrine disrupting contaminants (EDCs), metabolites and illicit drugs in a WWTW and environmental waters. Chemosphere 174, 437–446.

Ayan-Varela, M., Villar-Rodil, S., Paredes, J.I., Munuera, J.M., Pagan, A., Lozano-Perez, A.A., Cenis, J.L., Martinez-Alonso, A., Tascon, J.M., 2015. Investigating the dispersion behavior in solvents, biocompatibility, and use as support for highly efficient metal catalysts of exfoliated graphitic carbon nitride. ACS Appl. Mater. Interfaces 7 (43), 24032–24045.

Batmunkh, M., Bat-Erdene, M., Shapter, J.G., 2016. Phosphorene and phosphorene-based materials-prospects for future applications. Adv. Mater. 28 (39), 8586–8617.

Cao, S., Low, J., Yu, J., Jaroniec, M., 2015. Polymeric photocatalysts based on graphitic carbon nitride. Adv. Mater. 27 (13), 2150–2176.

Chang, C., Fu, Y., Hu, M., Wang, C., Shan, G., Zhu, L., 2013. Photodegradation of bisphenol A by highly stable palladium-doped mesoporous graphite carbon nitride (Pd/mpg-C_3N_4) under simulated solar light irradiation. Appl. Catal. B Environ. 142–143, 553–560.

Cheng, N., Tian, J., Liu, Q., Ge, C., Qusti, A.H., Asiri, A.M., Al-Youbi, A.O., Sun, X., 2013. Au-nanoparticle-loaded graphitic carbon nitride nanosheets: green photocatalytic synthesis and application toward the degradation of organic pollutants. ACS Appl. Mater. Interfaces 5 (15), 6815–6819.

Coleman, J.N., Lotya, M., O'Neill, A., Bergin, S.D., King, P.J., Khan, U., Young, K., Gaucher, A., De, S., Smith, R.J., Shvets, I.V., Arora, S.K., Stanton, G., Kim, H.Y., Lee, K., Kim, G.T., Duesberg, G.S., Hallam, T., Boland, J.J., Wang, J.J., Donegan, J.F., Grunlan, J.C., Moriarty, G., Shmeliov, A., Nicholls, R.J., Perkins, J.M., Grieveson, E.M., Theuwissen, K., McComb, D.W., Nellist, P.D., Nicolosi, V., 2011. Two-dimensional nanosheets produced by liquid exfoliation of layered materials. Science 331 (6017), 568–571.

Dong, F., Wang, Z., Sun, Y., Ho, W.K., Zhang, H., 2013. Engineering the nanoarchitecture and texture of polymeric carbon nitride semiconductor for enhanced visible light photocatalytic activity. J. Colloid Interface Sci. 401, 70–79.

Dong, F., Xiong, T., Sun, Y., Zhang, Y., Zhou, Y., 2015. Controlling interfacial contact and exposed facets for enhancing photocatalysis via 2D–2D heterostructures. Chem. Commun. (Camb.) 51 (39), 8249–8252.

Eswaraiah, V., Zeng, Q., Long, Y., Liu, Z., 2016. Black phosphorus nanosheets: synthesis, characterization and applications. Small 12 (26), 3480–3502.

Fang, Z., Liu, Y., Fan, Y., Ni, Y., Wei, X., Tang, K., Shen, J., Chen, Y., 2011. Epitaxial growth of CdS nanoparticle on Bi_2S_3 nanowire and photocatalytic application of the heterostructure. J. Phys. Chem. C 115 (29), 13968–13976.

Fei, X., Tan, H., Cheng, B., Zhu, B., Zhang, L., 2021. 2D/2D black phosphorus/g-C_3N_4 S-scheme heterojunction photocatalysts for CO_2 reduction investigated using DFT calculations. Acta Phys. -Chim. Sin. 37 (6), 2010027.

Guo, Q., Zhang, Y., Zhang, H.-S., Liu, Y., Zhao, Y.-J., Qiu, J., Dong, G., 2017. 3D foam strutted graphene carbon nitride with highly stable optoelectronic properties. Adv. Funct. Mater. 27 (42).

Han, C., Li, J., Ma, Z., Xie, H., Waterhouse, G.I.N., Ye, L., Zhang, T., 2018. Black phosphorus quantum dot/g-C_3N_4 composites for enhanced CO_2 photoreduction to CO. Sci. China Mater. 61 (9), 1159–1166.

He, R., Hua, J., Zhang, A., Wang, C., Peng, J., Chen, W., Zeng, J., 2017. Molybdenum disulfide-black phosphorus hybrid nanosheets as a superior catalyst for electrochemical hydrogen evolution. Nano Lett. 17 (7), 4311–4316.

He, D., Zhang, Z., Xing, Y., Zhou, Y., Yang, H., Liu, H., Qu, J., Yuan, X., Guan, J., Zhang, Y.-N., 2020. Black phosphorus/graphitic carbon nitride: a metal-free photocatalyst for "green" photocatalytic bacterial inactivation under visible light. Chem. Eng. J. 384.

He, D., Yang, H., Jin, D., Qu, J., Yuan, X., Zhang, Y.-N., Huo, M., Peijnenburg, W.J.G.M., 2021. Rapid water purification using modified graphitic carbon nitride and visible light. Appl. Catal. B Environ. 285.

Hernandez, Y., Nicolosi, V., Lotya, M., Blighe, F.M., Sun, Z., De, S., McGovern, I.T., Holland, B., Byrne, M., Gun'Ko, Y.K., Boland, J.J., Niraj, P., Duesberg, G., Krishnamurthy, S., Goodhue, R., Hutchison, J., Scardaci, V., Ferrari, A.C., Coleman, J.N., 2008. High-yield production of graphene by liquid-phase exfoliation of graphite. Nat. Nanotechnol. 3 (9), 563–568.

Hu, C., Yuchao, T., Lanyu, L., Zhengping, H., Yizhong, W., Hongxiao, T., 2004. Effects of inorganic anions on photoactivity of various photocatalysts under different conditions. J. Chem. Technol. Biotechnol. 79 (3), 247–252.

Hu, X., Hu, C., Peng, T., Zhou, X., Qu, J., 2010. Plasmon-induced inactivation of enteric pathogenic microorganisms with Ag-AgI/Al_2O_3 under visible-light irradiation. Environ. Sci. Technol. 44, 7058–7062.

Jiang, R., Lu, G., Yan, Z., Wu, D., Zhou, R., Bao, X., 2019. Insights into a CQD-$SnNb_2O_6$/BiOCl Z-scheme system for the degradation of benzocaine: influence factors, intermediate toxicity and photocatalytic mechanism. Chem. Eng. J. 374, 79–90.

Jiang, L., Yuan, X., Zeng, G., Liang, J., Chen, X., Yu, H., Wang, H., Wu, Z., Zhang, J., Xiong, T., 2018. In-situ synthesis of direct solid-state dual Z-scheme WO_3/g-C_3N_4/Bi_2O_3 photocatalyst for the degradation of refractory pollutant. Appl. Catal. B Environ. 227, 376–385.

Ju, E., Dong, K., Chen, Z., Liu, Z., Liu, C., Huang, Y., Wang, Z., Pu, F., Ren, J., Qu, X., 2016. Copper(II)-graphitic carbon nitride triggered synergy: improved ROS generation and reduced glutathione levels for enhanced photodynamic therapy. Angew. Chem. Int. Ed. Engl. 55 (38), 11467–11471.

Lewis, E.A., Brent, J.R., Derby, B., Haigh, S.J., Lewis, D.J., 2017. Solution processing of two-dimensional black phosphorus. Chem. Commun. (Camb.) 53 (9), 1445–1458.

Li, G., Nie, X., Chen, J., Jiang, Q., An, T., Wong, P.K., Zhang, H., Zhao, H., Yamashita, H., 2015. Enhanced visible-light-driven photocatalytic inactivation of *Escherichia coli* using g-C_3N_4/TiO_2 hybrid photocatalyst synthesized using a hydrothermal-calcination approach. Water Res. 86, 17–24.

Li, P., Li, J., Feng, X., Li, J., Hao, Y., Zhang, J., Wang, H., Yin, A., Zhou, J., Ma, X., Wang, B., 2019. Metal-organic frameworks with photocatalytic bactericidal activity for integrated air cleaning. Nat. Commun. 10 (1), 2177.

Liu, J.L., Wong, M.H., 2013. Pharmaceuticals and personal care products (PPCPs): a review on environmental contamination in China. Environ. Int. 59, 208–224.

Liu, H., Du, Y., Deng, Y., Ye, P.D., 2015. Semiconducting black phosphorus: synthesis, transport properties and electronic applications. Chem. Soc. Rev. 44 (9), 2732–2743.

Liu, C., Kong, D., Hsu, P.C., Yuan, H., Lee, H.W., Liu, Y., Wang, H., Wang, S., Yan, K., Lin, D., Maraccini, P.A., Parker, K.M., Boehm, A.B., Cui, Y., 2016. Rapid water disinfection using vertically aligned MoS_2 nanofilms and visible light. Nat. Nanotechnol. 11 (12), 1098–1104.

Low, J., Cao, S., Yu, J., Wageh, S., 2014. Two-dimensional layered composite photocatalysts. Chem. Commun. (Camb.) 50 (74), 10768–10777.

Ma, S., Zhan, S., Jia, Y., Shi, Q., Zhou, Q., 2016. Enhanced disinfection application of Ag-modified g-C_3N_4 composite under visible light. Appl. Catal. B Environ. 186, 77–87.

Martin, D.J., Qiu, K., Shevlin, S.A., Handoko, A.D., Chen, X., Guo, Z., Tang, J., 2014. Highly efficient photocatalytic H_2 evolution from water using visible light and structure-controlled graphitic carbon nitride. Angew. Chem. Int. Ed. Engl. 53 (35), 9240–9245.

Meng, A., Tian, W., Yang, H., Wang, X., Wang, X., Li, Z., 2021. Molybdenum sulfide-modified metal-free graphitic carbon nitride/black phosphorus photocatalyst synthesized via high-energy ball-milling for efficient hydrogen evolution and hexavalent chromium reduction. J. Hazard. Mater. 413, 125400.

Moniz, S.J.A., Shevlin, S.A., Martin, D.J., Guo, Z.-X., Tang, J., 2015. Visible-light driven heterojunction photocatalysts for water splitting-a critical review. Energy Environ. Sci. 8 (3), 731–759.

Mostafa, S., Rosario-Ortiz, F.L., 2013. Singlet oxygen formation from wastewater organic matter. Environ. Sci. Technol. 47 (15), 8179–8186.

Mu, Y., Si, M.S., 2015. The mechanical exfoliation mechanism of black phosphorus to phosphorene: a first-principles study. EPL (Europhysics Letters) 112 (3).

Nosaka, Y., Nosaka, A.Y., 2017. Generation and detection of reactive oxygen species in photocatalysis. Chem. Rev. 117 (17), 11302–11336.

Ong, W.J., Tan, L.L., Ng, Y.H., Yong, S.T., Chai, S.P., 2016. Graphitic carbon nitride (g-C_3N_4)-based photocatalysts for artificial photosynthesis and environmental remediation: are we a step closer to achieving sustainability? Chem. Rev. 116 (12), 7159–7329.

Qiu, P., Xu, C., Zhou, N., Chen, H., Jiang, F., 2018. Metal-free black phosphorus nanosheets-decorated graphitic carbon nitride nanosheets with C-P bonds for excellent photocatalytic nitrogen fixation. Appl. Catal. B Environ. 221, 27–35.

Ran, J., Zhu, B., Qiao, S.Z., 2017. Phosphorene co-catalyst advancing highly efficient visible-light photocatalytic hydrogen production. Angew. Chem. Int. Ed. Engl. 56 (35), 10373–10377.

Shang, E., Li, Y., Niu, J., Zhou, Y., Wang, T., Crittenden, J.C., 2017. Relative importance of humic and fulvic acid on ROS generation, dissolution, and toxicity of sulfide nanoparticles. Water Res. 124, 595–604.

da Silva, G.T.S.T., Carvalho, K.T.G., Lopes, O.F., Ribeiro, C., 2017. G-C_3N_4/Nb_2O_5 heterostructures tailored by sonochemical synthesis: enhanced photocatalytic performance in oxidation of emerging pollutants driven by visible radiation. Appl. Catal. B Environ. 216, 70–79.

Sui, Q., Gebhardt, W., Schroder, H.F., Zhao, W., Lu, S., Yu, G., 2017. Identification of new oxidation products of bezafibrate for better understanding of its toxicity evolution and oxidation mechanisms during ozonation. Environ. Sci. Technol. 51 (4), 2262–2270.

Sun, L., Du, T., Hu, C., Chen, J., Lu, J., Lu, Z., Han, H., 2017. Antibacterial activity of graphene oxide/g-C_3N_4 composite through photocatalytic disinfection under visible light. ACS Sustain. Chem. Eng. 5 (10), 8693–8701.

Sun, P., Liu, H., Feng, M., Guo, L., Zhai, Z., Fang, Y., Zhang, X., Sharma, V.K., 2019. Nitrogen-sulfur co-doped industrial graphene as an efficient peroxymonosulfate activator: singlet oxygen-dominated catalytic degradation of organic contaminants. Appl. Catal. B Environ. 251, 335–345.

Sun, H., Qin, P., Wu, Z., Liao, C., Guo, J., Luo, S., Chai, Y., 2020. Visible light-driven photocatalytic degradation of organic pollutants by a novel Ag_3VO_4/Ag_2CO_3 p-n heterojunction photocatalyst: mechanistic insight and degradation pathways. J. Alloys Compd. 834, 155211.

Vazquez, G., Alvarez, E., Navaza, J.M., 1995. Surface tension of alcohol water from 20 to 50°C. J. Chem. Eng. Data 40, 611–614.

Wang, W., Yu, J.C., Xia, D., Wong, P.K., Li, Y., 2013. Graphene and g-C_3N_4 nanosheets cowrapped elemental alpha-sulfur as a novel metal-free heterojunction photocatalyst for bacterial inactivation under visible-light. Environ. Sci. Technol. 47 (15), 8724–8732.

Wang, H., Yang, X., Shao, W., Chen, S., Xie, J., Zhang, X., Wang, J., Xie, Y., 2015. Ultrathin black phosphorus nanosheets for efficient singlet oxygen generation. J. Am. Chem. Soc. 137 (35), 11376–11382.

Wang, L., Xu, Q., Xu, J., Weng, J., 2016. Synthesis of hybrid nanocomposites of ZIF-8 with two-dimensional black phosphorus for photocatalysis. RSC Adv. 6 (73), 69033–69039.

Wang, F., Chen, P., Feng, Y., Xie, Z., Liu, Y., Su, Y., Zhang, Q., Wang, Y., Yao, K., Lv, W., Liu, G., 2017. Facile synthesis of N-doped carbon dots/g-C_3N_4 photocatalyst with enhanced visible-light photocatalytic activity for the degradation of indomethacin. Appl. Catal. B Environ. 207, 103–113.

Wang, F., Wang, Y., Feng, Y., Zeng, Y., Xie, Z., Zhang, Q., Su, Y., Chen, P., Liu, Y., Yao, K., Lv, W., Liu, G., 2018a. Novel ternary photocatalyst of single atom-dispersed silver and carbon quantum dots co-loaded with ultrathin g-C_3N_4 for broad spectrum photocatalytic degradation of naproxen. Appl. Catal. B Environ. 221, 510–520.

Wang, W., Li, G., An, T., Chan, D.K.L., Yu, J.C., Wong, P.K., 2018b. Photocatalytic hydrogen evolution and bacterial inactivation utilizing sonochemical-synthesized g-C_3N_4/red phosphorus hybrid nanosheets as a wide-spectral-responsive photocatalyst: the role of type I band alignment. Appl. Catal. B Environ. 238, 126–135.

Wang, F., Wang, Y., Wu, Y., Wei, D., Li, L., Zhang, Q., Liu, H., Liu, Y., Lv, W., Liu, G., 2019. Template-free synthesis of oxygen-containing ultrathin porous carbon quantum dots/g-C_3N_4 with superior photocatalytic activity for PPCPs remediation. Environ. Sci. Nano 6 (8), 2565–2576.

Wu, Z., Wang, Y., Xiong, Z., Ao, Z., Pu, S., Yao, G., Lai, B., 2020. Core-shell magnetic Fe_3O_4@Zn/Co-ZIFs to activate peroxymonosulfate for highly efficient degradation of carbamazepine. Appl. Catal. B Environ. 277.

Xiong, J., Li, X., Huang, J., Gao, X., Chen, Z., Liu, J., Li, H., Kang, B., Yao, W., Zhu, Y., 2020. CN/rGO@BPQDs high-low junctions with stretching spatial charge separation ability for photocatalytic degradation and H_2O_2 production. Appl. Catal. B Environ. 266.

Xue, J., Ma, S., Zhou, Y., Zhang, Z., He, M., 2015. Facile photochemical synthesis of Au/Pt/g-C_3N_4 with plasmon-enhanced photocatalytic activity for antibiotic degradation. ACS Appl. Mater. Interfaces 7 (18), 9630–9637.

Yang, S., Gong, Y., Zhang, J., Zhan, L., Ma, L., Fang, Z., Vajtai, R., Wang, X., Ajayan, P.M., 2013. Exfoliated graphitic carbon nitride nanosheets as efficient catalysts for hydrogen evolution under visible light. Adv. Mater. 25 (17), 2452–2456.

Yang, Y., Ok, Y.S., Kim, K.H., Kwon, E.E., Tsang, Y.F., 2017. Occurrences and removal of pharmaceuticals and personal care products (PPCPs) in drinking water and water/sewage treatment plants: a review. Sci. Total Environ. 596–597, 303–320.

Yang, L., Zhan, Y., Gong, Y., Ren, E., Lan, J., Guo, R., Yan, B., Chen, S., Lin, S., 2021. Development of eco-friendly CO_2-responsive cellulose nanofibril aerogels as "green" adsorbents for anionic dyes removal. J. Hazard. Mater. 405, 124194.

Zhang, W., An, T., Cui, M., Sheng, G., Fu, J., 2005. Effects of anions on the photocatalytic and photoelectrocatalytic degradation of reactive dye in a packed-bed reactor. J. Chem. Technol. Biotechnol. 80 (2), 223–229.

Zhang, L.S., Wong, K.H., Yip, H.Y., Hu, C., Yu, J.C., Chan, C.Y., Wong, P.K., 2010. Effective photocatalytic disinfection of E. coli K-12 using AgBr-Ag-Bi_2WO_6 nanojunction system irradiated by visible light: the role of diffusing hydroxyl radicals. Environ. Sci. Technol. 44, 1392–1398.

Zhang, X., Xie, X., Wang, H., Zhang, J., Pan, B., Xie, Y., 2013a. Enhanced photoresponsive ultrathin graphitic-phase C_3N_4 nanosheets for bioimaging. J. Am. Chem. Soc. 135 (1), 18–21.

Zhang, Z., Shao, C., Li, X., Sun, Y., Zhang, M., Mu, J., Zhang, P., Guo, Z., Liu, Y., 2013b. Hierarchical assembly of ultrathin hexagonal SnS_2 nanosheets onto electrospun TiO_2 nanofibers: enhanced photocatalytic activity based on photoinduced interfacial charge transfer. Nanoscale 5 (2), 606–618.

Zhang, Q., Chen, P., Tan, C., Chen, T., Zhuo, M., Xie, Z., Wang, F., Liu, H., Cai, Z., Liu, G., Lv, W., 2018a. A photocatalytic degradation strategy of PPCPs by a heptazine-based CN organic polymer (OCN) under visible light. Environ. Sci. Nano 5 (10), 2325–2336.

Zhang, Q., Chen, P., Zhuo, M., Wang, F., Su, Y., Chen, T., Yao, K., Cai, Z., Lv, W., Liu, G., 2018b. Degradation of indometacin by simulated sunlight activated CDs-loaded $BiPO_4$ photocatalyst: roles of oxidative species. Appl. Catal. B Environ. 221, 129–139.

Zhang, Q., Tan, C., Zheng, X., Chen, P., Zhuo, M., Chen, T., Xie, Z., Wang, F., Liu, H., Liu, Y., Zhang, X., Lv, W., Liu, G., 2019. Dual metal-free polymer reactive sites for the efficient degradation of diclofenac by visible light-driven oxygen reduction to superoxide radical and hydrogen peroxide. Environ. Sci. Nano 6 (8), 2577–2590.

Zhao, Y., Kuang, J., Zhang, S., Li, X., Wang, B., Huang, J., Deng, S., Wang, Y., Yu, G., 2017. Ozonation of indomethacin: kinetics, mechanisms and toxicity. J. Hazard. Mater. 323, 460–470.

Zhao, Q., Ma, W., Pan, B., Zhang, Q., Zhang, X., Zhang, S., Xing, B., 2018. Wrinkle-induced high sorption makes few-layered black phosphorus a superior adsorbent for ionic organic compounds. Environ. Sci. Nano 5 (6), 1454–1465.

Zheng, Y., Yu, Z., Ou, H., Asiri, A.M., Chen, Y., Wang, X., 2018. Black phosphorus and polymeric carbon nitride heterostructure for photoinduced molecular oxygen activation. Adv. Funct. Mater. 28 (10).

Zheng, Y., Chen, Y., Gao, B., Lin, B., Wang, X., 2020a. Black phosphorus and carbon nitride hybrid photocatalysts for photoredox reactions. Adv. Funct. Mater. 30 (30).

Zheng, X., Zhang, Q., Chen, T., Wu, Y., Hao, J., Tan, C., Chen, P., Wang, F., Liu, H., Lv, W., Liu, G., 2020b. A novel synthetic carbon and oxygen doped stalactite-like g-C_3N_4 for broad-spectrum-driven indometacin degradation. J. Hazard. Mater. 386, 121961.

Zhou, Y., Yu, M., Liang, H., Chen, J., Xu, L., Niu, J., 2021. Novel dual-effective Z-scheme heterojunction with g-C_3N_4, Ti_3C_2 MXene and black phosphorus for improving visible light-induced degradation of ciprofloxacin. Appl. Catal. B Environ. 291, 120105.

Zhu, M., Kim, S., Mao, L., Fujitsuka, M., Zhang, J., Wang, X., Majima, T., 2017. Metal-free photocatalyst for H_2 evolution in visible to near-infrared region: black phosphorus/graphitic carbon nitride. J. Am. Chem. Soc. 139 (37), 13234–13242.

Zhu, X., Zhang, T., Jiang, D., Duan, H., Sun, Z., Zhang, M., Jin, H., Guan, R., Liu, Y., Chen, M., Ji, H., Du, P., Yan, W., Wei, S., Lu, Y., Yang, S., 2018. Stabilizing black phosphorus nanosheets via edge-selective bonding of sacrificial C_{60} molecules. Nat. Commun. 9 (1), 4177.